International Journal of Plasticity 159 (2022) 103476

Contents lists available at ScienceDirect

International Journal of Plasticity

journal homepage: www.elsevier.com/locate/ijplas

Twin and dislocation induced grain subdivision and strengthening in laser shock peened Ti

Xuan Huang [a,b], Wenxin Zhu [b], Kai Chen [b,*], R. Lakshmi Narayan [c], Upadrasta Ramamurty [d,e], Liucheng Zhou [a,f,**], Weifeng He [a,f]

[a] *State Key Laboratory for Manufacturing and Systems Engineering, Xi'an Jiaotong University, Xi'an, Shaanxi 710049, China*
[b] *Center for Advancing Materials Performance from the Nanoscale (CAMP-Nano), State Key Laboratory for Mechanical Behavior of Materials, Xi'an Jiaotong University, Xi'an, Shaanxi 710049, China*
[c] *Department of Materials Science and Engineering, Indian Institute of Technology, Delhi, New Delhi 110016, India*
[d] *School of Mechanical and Aerospace Engineering, Nanyang Technological University, Singapore 639798, Singapore*
[e] *Institute of Materials Research and Engineering, Agency for Science, Technology and Research, 2 Fusionopolis Way, Singapore 138634, Republic of Singapore*
[f] *Science and Technology on Plasma Dynamics Laboratory, Air Force Engineering University, Xi'an, Shaanxi 710038, China*

ARTICLE INFO

Keywords:
Laser shock peening
Microstructural gradient
Grain subdivision
Twin-twin intersections
EBSD data mining

ABSTRACT

A significantly refined microstructure with high twin and dislocation densities is a common feature in the Ti surface layers subjected to laser shock peening (LSP). In this study, in order to develop a detailed understanding of the different twin variants and accurate estimation of twin and dislocation densities that result from LSP, electron backscatter diffraction (EBSD) and transmission electron microscopy (TEM) were performed at different depths below the peened surfaces of single and triple LSP impacted Ti. To overcome challenges associated with characterization of the nano-sized LSP-induced twins during the conventional EBSD analysis, a novel data mining strategy is developed to identify the characteristic straight twin boundary traces from the band contrast maps. Results show five types of twins, whose total density initially increases and then monotonically decreases with increasing distance from the LSP treated surface. The intersection of the primary and secondary type twins subdivides the grains and leads to grain refinement. In contrast, the dislocation density is highest at the LSP treated surface but decreases monotonically with the increasing depth. A similar trend in the variation of microhardness as a function of the depth indicates that LSP-induced strengthening is dominated by the dislocations and grain refinement. Further analysis reveals that the former's contribution is more pronounced than that of the latter. The understanding developed in this work can be useful for the design of the alloys and the LSP process for improved mechanical performance.

1. Introduction

Ti and its alloys are widely used as aero-engine fan/compressor blades due to their high specific strength, excellent intermediate

* Corresponding author.
** Corresponding author at: State Key Laboratory for Mechanical Behavior of Materials, Xi'an Jiaotong University, 28 West Xianning Rd, Xi'an, Shaanxi 710049, China

E-mail addresses: kchenlbl@gmail.com (K. Chen), happyzlch@163.com (L. Zhou).

https://doi.org/10.1016/j.ijplas.2022.103476
Received 22 August 2022; Received in revised form 20 October 2022;
Available online 6 November 2022
0749-6419/

temperature performance, and exceptional corrosion resistance (Lütjering and Williams, 2007; Kumar and Ramamurty, 2020; Singh and Ramamurty, 2020; Xiong et al., 2020; Sahu et al., 2022). For enhancing the fatigue strength of Ti components (Joseph et al., 2018; Zhao et al., 2020), laser shock peening (LSP) has been developed as a surface hardening technique, which introduces compressive residual stresses and microstructural refinement (Spanrad and Tong, 2011; Luo et al, 2018; Sun et al., 2018; Fu et al., 2022). The residual stresses can relax during the elevated temperature service and/or cyclic loads (Lou et al., 2016). Likewise, there is a possibility for some of the microstructural features to evolve with service time and temperature. Therefore, a detailed understanding of the LSP induced plastic deformation and microstructural evolution is essential. Such an understanding can then be utilized to guide the design of the alloys and LSP process to improve the performance and reliability.

Both dislocations and mechanical twins play an important role in accommodating the plastic deformation in Ti alloys (Morrow et al., 2016; Tang et al., 2020). A high-density of dislocations and dislocation cells were observed in them upon LSP. In turn, they contribute to the nanocrystallization of the alloy near the peened surface (Zhou et al., 2013; Nie et al., 2014; Lou et al., 2016). However, prior studies on the twinning behavior in the LSP treated Ti show significant discrepancies or even contradictions in terms of twin density, spatial distribution, size, and type. For example, a high density of needle-shaped twins, with widths of tens of nanometers, was observed under transmission electron microscope (TEM) in some LSP treated Ti alloys (Ren et al., 2015), while only a few nano-sized twins were reported in another instance (Lainé et al., 2017). Even those twins in the latter case are invisible under the electron backscatter diffraction (EBSD) mode of imaging, probably because of their fine size (Lainé et al., 2017). The spatial distribution and the evolution of dislocation density along the shock propagation direction are also contested topics. While one study shows that the mechanical twins exist only to a depth of 10 μm from the surface (Lainé et al., 2017), another reports relatively fewer mechanical twins closer to the surface compared to the subsurface regions of 100 – 200 μm depth (Yang et al., 2017). Moreover, the reported widths of the twins vary greatly, from nanosize to micron-scale, but the twin type was not reported (Ren et al., 2015; Lainé et al., 2017; Yang et al., 2017). In another study, the mechanical twins in pure Ti subjected to one LSP impact were identified to be $\{10\bar{1}1\}\langle\bar{1}012\rangle$ type from the selected area electron diffraction (SAED) pattern obtained (Lu et al., 2017). However, detailed crystallographic characterization of the twin-twin interactions, which greatly influence the microstructure refinement and grain boundary misorientation angles and directions, was not reported.

Due to its spatial resolution and capability for crystallographic analysis, TEM is the principal choice for mechanical twin characterization in the prior studies on the LSP Ti and its alloys. However, the probed area using TEM (μm scale) is about three orders of magnitude smaller than the LSP affected depth (mm scale). Hence, whether the TEM observation of the $\{10\bar{1}1\}\langle\bar{1}012\rangle$ twin type by Lu et al. (2017) is typical or unique for laser shock peened Ti is uncertain. While performing TEM on the specimens that are extracted from several different depths of the LSP affected surface can circumvent this problem, it requires considerable amount of time and effort. In contrast, one can cover much larger sampling area using the EBSD technique with the crystallographic orientation mapping capability. Although EBSD has been applied to reveal the twin types in Ti subjected to shock (Xu et al., 2019), the Kikuchi patterns obtained from alloys that are severely deformed (as in the case of the LSP layers) are difficult to index (Chun et al., 2005; Wang et al., 2018). Moreover, the fine twin structures may not be amenable to resolution and accurate assessment (Levinson et al., 2013).

Keeping the above constraints in mind, a novel data mining approach is developed in this work to discern the narrow mechanical twins with low indexing ratios from the EBSD scans. Using it, the microstructural features of pure Ti subjected to single and three LSP impacts are studied. Five different twin systems were identified from the EBSD scans, which provide a comprehensive understanding of the twin structures in the laser shock peened Ti. Importantly, the present study shows that the contradictory observations of the twins made in prior studies were a consequence of the smaller areas/volumes probed. The densities of the mechanical twins and dislocations are quantified as a function of the LSP impacts and depth of the peened layer. While the dislocation density decreases monotonically from the surface to the interior, the peak twin density appears in the sub-surface region. Boundaries of the individual primary twins, intersections of the primary-primary twins, and impingements of the primary and secondary twins are studied in detail. All these allow for a greater understanding of the subdivision of grains during LSP. The influence of microstructural features on the microhardness gradation is discussed.

2. Materials and methods

2.1. Materials

The as-received rolled Ti plate (commercial designation: TA1) is 5 mm thick. Its nominal composition is given in Table 1. Before LSP, it was annealed at 790 °C for 4 h and air cooled to obtain nominally dislocation-free equiaxed grains, whose size ranges between 20 and 100 μm. The microstructure of the annealed alloy is shown in the inverse pole figure (IPF) map obtained along the normal (to the rolling) direction (ND) in Fig. 1(a). The distribution in the grain misorientation angles displayed in Fig. 1(b) indicates that no preference for any particular misorientation angle. The microstructure is also devoid of annealing or growth twins. The pole figures displayed in Fig. 1(c) show that the crystallographic *c*-axes of the grains are inclined at about 30° from ND towards the transverse

Table 1
Nominal composition of the TA1 grade Ti alloy (in wt. %) (Zhang and Li, 2017).

Fe	C	N	H	O	Ni	Ti
0.25	0.10	0.03	0.015	0.30	0.20	Balance

direction (TD), which is one of the typical textures of Ti (Wang et al., 2018). The $(2\overline{1}\overline{1}0)$ plane normal is close to the rolling direction (RD).

2.2. LSP treatments

Two samples (22, 15, and 5 mm long along TD, RD, and ND, respectively) were cut from the annealed Ti plate. The RD-TD surfaces of both the specimens were polished to mirror finish with SiC papers of different grades, cleaned, and then laser shock peened using a custom developed apparatus that was equipped with a Q-switched Nd:YAG laser with the wavelength of 1064 nm and pulse width of 20 ns. For LSP, a laser beam with a focal diameter of 2.2 mm with an energy of 4 J was applied. A 100-μm-thick aluminum tape was employed as the absorbing layer to protect the surfaces of the Ti specimens from direct ablation and to promote a better coupling with the laser energy. The whole specimen, together with the aluminum tape, was submerged in a water bath to a depth of about 1 mm below the surface, which was used to confine the diffusion of the high temperature plasma induced by laser irradiation and to increase the pressure of the shock wave (Zhou et al., 2016), which propagates along the ND. A schematic illustrating the LSP process was shown in Fig. 2(a). The specimens were laser shock peened by either one or three impacts, both with a 50% overlap between adjacent laser beam scanning positions. The numbers of impacts were selected based on prior experimental studies, which show that significant microstructural (and hence mechanical property) changes in Ti would accrue just after one impact of LSP and saturate after about three impacts (Nie et al., 2014; Nie et al., 2014).

2.3. Microstructure characterization

The microstructural features of the LSP treated specimens were characterized on the ND-TD plane along the shock wave propagation direction (ND) from the surface to the interior using the Oxford Instruments EBSD system, as shown in Fig. 2(b). Prior to it, the cross-section was mechanically ground with SiC paper (P#2400 of the European standard as the final step), and then electropolished at 50 V/0.4 A for about 60 s in a mixed solution of 10% perchloric acid and 90% glacial acetic acid. All the EBSD scans were conducted with a step size of 0.4 μm in electron-ion dual beam system (Helios Nanolab 600) equipped with an area detector to record the Kikuchi

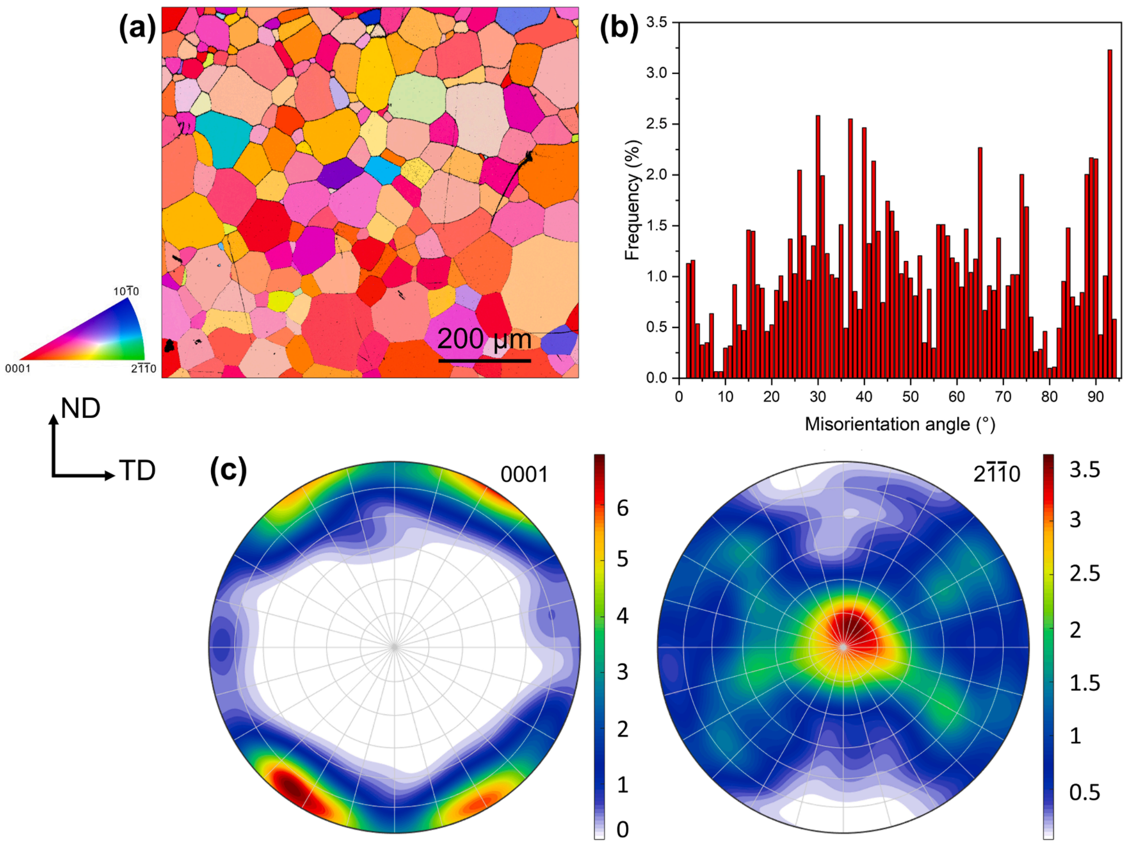

Fig. 1. Microstructure of the TA1 grade Ti alloy after 790 °C annealing characterized using EBSD. The IPF map (a) and misorientation angle distribution histogram (b) suggest no grain boundary type preference and non-existence of annealing or growth twins. The pole figures (c) illustrate strong texture which is typical in Ti.

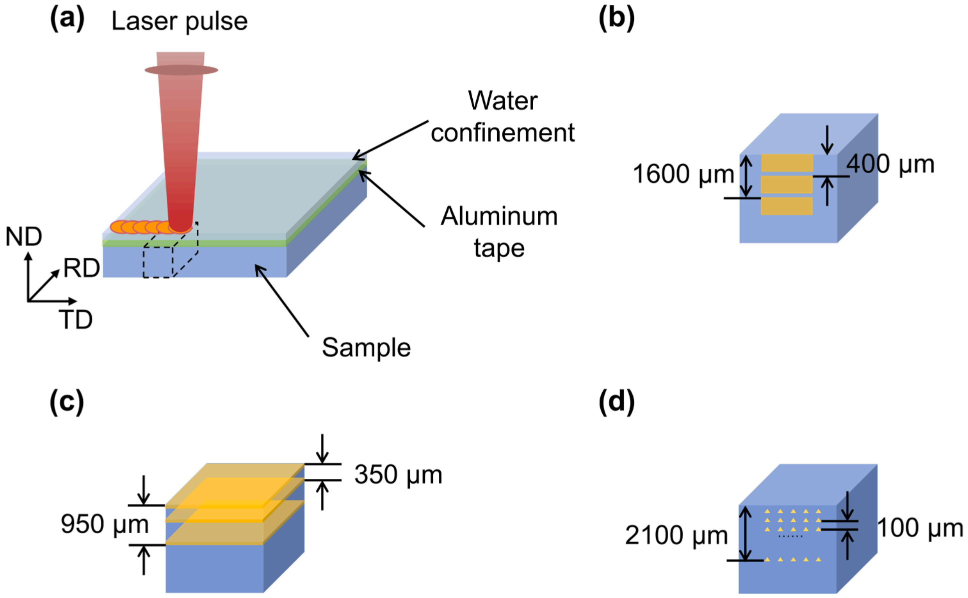

Fig. 2. Schematic diagram of (a) LSP processing, (b) EBSD characterization, (c) TEM thin foil preparations and (d) microhardness measurements.

patterns. The acceleration voltage of the electron-beam was 20 kV. The software packages, Aztec (developed by Oxford Instruments) and an in-house developed one (XtalCAMP (Li et al., 2020)), were employed for data acquisition and analysis. Kernel average misorientation (KAM), defined as the mean angle between the crystallographic orientation of each pixel and those of its eight nearest neighbors (Clair et al., 2011; Tiamiyu et al., 2018), was applied to calculate the dislocation densities quantitatively (Pantleon, 2008). To identify the twin boundaries from the EBSD maps, a novel data mining approach was developed (described in detail in Section 2.4) and used.

The TEM specimens were sectioned parallel to the RD-TD plane from the LSP-affected zones, as shown in Fig. 2(c), ground to a thickness of less than 100 μm, cut into 3 mm diameter discs, and sequentially thinned down to about 50 μm. Finally, electron transparent foils were prepared by twin-jet electropolishing with a solution of 5% perchloric acid, 35% butanol, and 60% methanol. The TEM characterization was carried out on a JEM-2100F electron microscope.

The micro-hardness measurements on the ND-TD cross-sectional plane of the annealed and laser shock peened specimens shown in Fig. 2(d) were conducted using a Vickers digital micro-hardness tester (HXD-1000TMC/LCD) at a constant loading rate of 0.035 mm/s. The load was held at the peak load of 100 g for 10 s. 21 points were measured with an interval of 100 μm between them along a straight line parallel to the ND from the top surface. Five hardness measurements were performed at each depth.

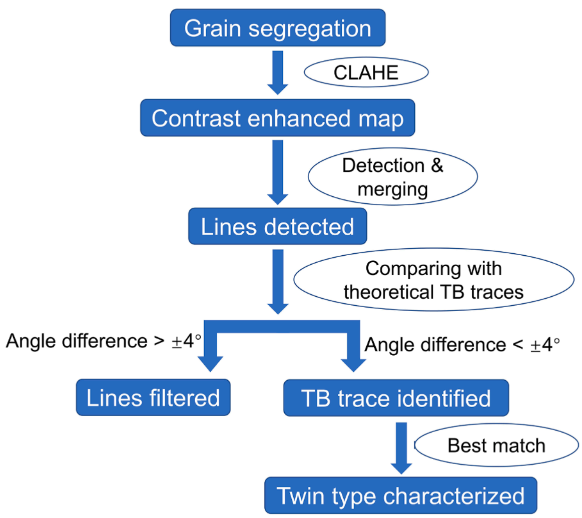

Fig. 3. The flow diagram showing how the twin boundary fraction and type are characterized.

2.4. EBSD data mining

A new EBSD data mining method was developed in this study to count the twin boundary fraction and characterize the twin type. To overcome the difficulties caused by the low signal-to-noise ratio of the EBSD band contrast maps, line segmentation and false twin boundary identification, the following procedure illustrated in the flowchart displayed in Fig. 3 was performed. The details of the algorithm are provided below.

The image of a typical grain in the LSP affected zone is displayed in Fig. 4. The IPF image (Fig. 4(a)) shows only one orientation in it, with no twins but only a few pixels with different orientation in the region that could not be indexed successfully. In the regions that could be mapped well, unequivocal identification of the twin boundaries with twin plane and direction was possible through the calculation of the misorientation angle and axis between each adjacent pair of pixels, as we reported in a prior study (Li et al., 2015). Unfortunately, this method is not applicable to the case shown here. As shown in Fig. 4(b), straight linear shapes with dark contrast, which are characteristic of the mechanical twins, were observed in the band contrast map of the same area output by the Aztec software. Interestingly, some of the dark lines in it correspond to the unindexed pixels, while some others were even invisible in Fig. 4 (a), probably because the twinning lamellae are so thin that their diffraction signals were overwhelmed completely by those of the matrix. This observation also highlights the need for a new identification strategy of the twins, based on the maps of band contrast rather than the crystallographic orientation. Such a strategy is described below.

First, each grain was segregated using the region growing algorithm (Rolf Adams, 1994). Once a seed pixel was chosen inside the grain in the band contrast image, its neighboring pixels with similar gray values were considered to be the same grain. To reduce the influence caused by contrast variation in each individual grain and simultaneously enhance the local contrast of the detailed microstructures at the intra-granular level, contrast limited adaptive histogram equalization (CLAHE) (Zuiderveld, 1994) was employed. Fig. 4(c) illustrates that the visualization of the linear structures improved significantly after such CLAHE process.

After the pre-treatment of grain segregation and contrast enhancement, twin boundaries were identified by performing line detection, using a method inspired by the classic and parameter-free Line Segment Detector approach (Grompone Von Gioi et al.,

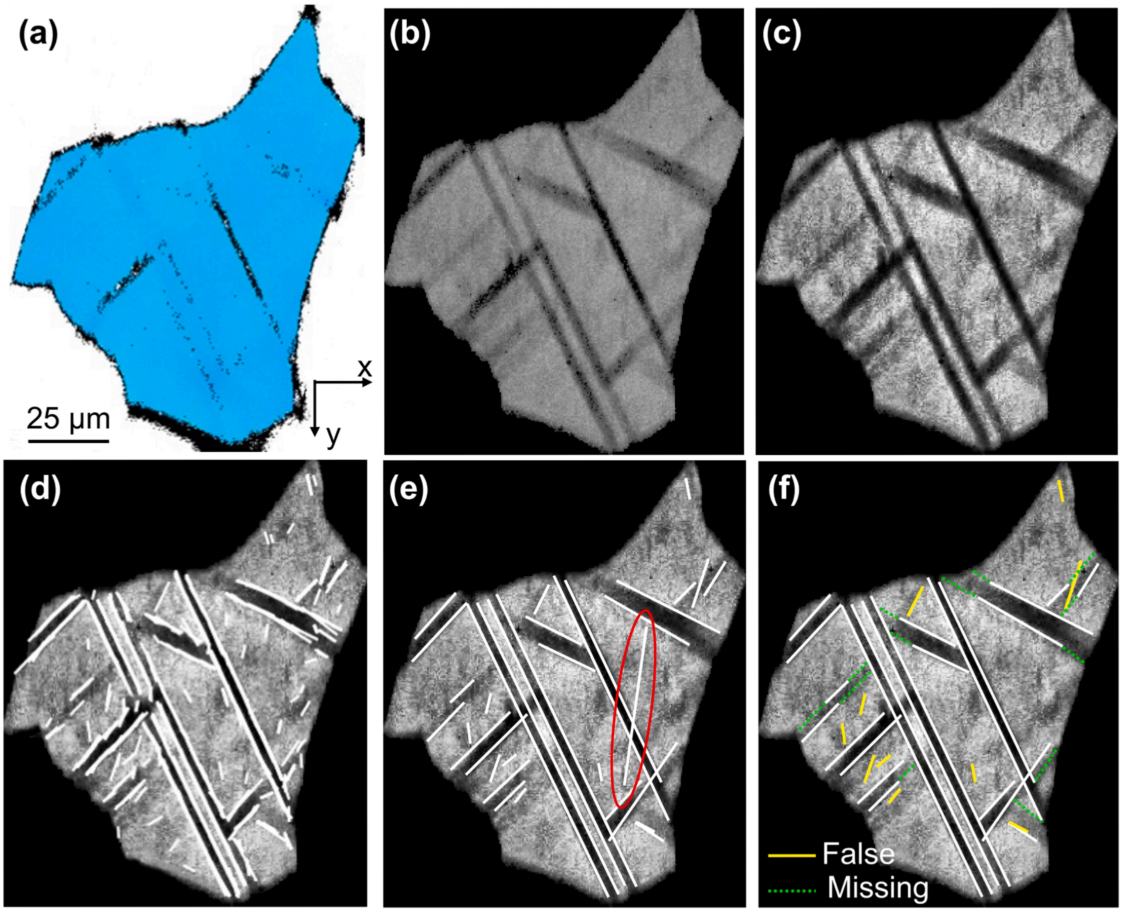

Fig. 4. EBSD data mining to identify twin traces. The IPF along the x-axis (a), band contrast map (b), and contrast enhanced map (c) show single orientation but straight line shaped contrast. Straight lines were (d) detected by Line segment detector approach and then (e) merged under the angular- and spatial-proximity criteria. (f) The detected twin boundaries were plotted, with false and missing ones marked in different colors.

2012). First, the gray-scale gradients in both x- and y-directions, $g_x(x, y)$ and $g_y(x, y)$, were computed for Pixel *(x,y)*:

$$g_x(x, y) = \frac{i(x+1,y) + i(x+1,y+1) - i(x,y) - i(x,y+1)}{2}, \textit{ and} \tag{1}$$

$$g_y(x, y) = \frac{i(x,y+1) + i(x+1,y+1) - i(x,y) - i(x+1,y)}{2}, \tag{2}$$

where i denotes intensity. Then, two quantities, angle of level-line $\alpha(x,y)$ and gradient magnitude $M(x,y)$, were defined:

$$\alpha(x,y) = arctan\left(\frac{g_x(x,y)}{-g_y(x,y)}\right), \text{ and} \tag{3}$$

$$M(x,y) = \sqrt{g_x^2(x,y) + g_y^2(x,y)}\ . \tag{4}$$

Pixels with M higher than a certain threshold value were defined as the valid ones and sorted into groups according to the M value from high to low. Starting from a seed pixel from the first group, a region growing algorithm was applied to construct the so-called line-support regions. Recursively, the valid neighbors of the pixels already in the line-support region were tried out, and those whose $\alpha(x,y)$ equaled the angle of region α_{region} up to a tolerance δ were added to the region. The initial α_{region} was set to $\alpha(x,y)$ of the seed pixel, and each time a new pixel was added to the region, it was updated to:

$$\alpha_{region} = arctan\left(\frac{\sum_j \sin\alpha(x,y)_j}{\sum_j \cos\alpha(x,y)_j}\right). \tag{5}$$

By testing all the valid pixels from higher to lower ordered groups, all the detected line segments in this example grain were plotted in Fig. 4(d). It was found that this approach tends to break the perceptually single line into multiple segments or detect two (almost) parallel segments for an individual line. To solve this problem, line segment merging (Hamid and Khan, 2016) method was applied. It is known that perception of mergeability of a pair of line segments is inversely proportional to their slope difference and spatial distance, but proportional to the length of the longer segment (Hamid and Khan, 2016). Hence, the following merging procedure was executed. First, the detected line segments were sequenced by length in the descending order. For the longest line segment L_1, a set of segments, P_{L_1}, was established by setting the following angular-proximity criterion:

$$P_{L_1} = [\forall L_2 \in L : (|\alpha_2 - \alpha_1| < \tau_\alpha)], \tag{6}$$

where L_2 represents any line segment that fulfilled this criterion, τ_α is a custom-defined angular tolerance, and α_1 and α_2 are the angles of L_1 and L_2, respectively. Then, the set P_{L_1} is further filtered according to the spatial distance between the line segment pair. Denoting (x_1,y_1), (x_2,y_2), (x_3,y_3), and (x_4,y_4) the coordinates of the start- and end-points of L_1 and L_2, respectively, the spatial-proximity criteria were checked sequentially in both horizontal and vertical directions in the following manner (Hamid and Khan, 2016):

$$\boldsymbol{P_{L_1}} = \begin{bmatrix} \forall \boldsymbol{L_2} \in \boldsymbol{P_{L_1}} : |\boldsymbol{x}_1 - \boldsymbol{x}_3| < \boldsymbol{\tau_h} \vee |\boldsymbol{x}_1 - \boldsymbol{x}_4| < \boldsymbol{\tau_h} \vee |\boldsymbol{x}_2 - \boldsymbol{x}_3| < \boldsymbol{\tau_h} \\ \vee|\boldsymbol{x}_2 - \boldsymbol{x}_4| < \boldsymbol{\tau_h} \end{bmatrix}, \tag{7}$$

$$\boldsymbol{P_{L_1}} = \begin{bmatrix} \forall \boldsymbol{L_2} \in \boldsymbol{P_{L_1}} : |\boldsymbol{y}_1 - \boldsymbol{y}_3| < \boldsymbol{\tau_v} \vee |\boldsymbol{y}_1 - \boldsymbol{y}_4| < \boldsymbol{\tau_v} \vee |\boldsymbol{y}_2 - \boldsymbol{y}_3| < \boldsymbol{\tau_v} \\ \vee|\boldsymbol{y}_2 - \boldsymbol{y}_4| < \boldsymbol{\tau_v} \end{bmatrix}. \tag{8}$$

In Eqs. (7) and (8), the distance tolerance τ_h and τ_v are user defined. By this method, all segments that could be merged with L_1 were categorized into $\boldsymbol{P_{L_1}}$. By traversing all the lines detected in the previous step, the repeated and/or broken line segments were reduced effectively, as demonstrated through Fig. 4(e).

It was noted that some of the lines, such as the one highlighted by the red ellipse in Fig. 4(e), were still mistakenly picked even after line segment merging, mainly due to the noise in the contrast map. Since the aim of this study is to investigate the density and distribution of twins, the detected line segments were further verified using the crystallographic rules. Since the twins and the parent grain share the same crystallographic plane (twin plane), all the possible twin boundary traces can be deduced according to the relations that were espoused in literature as well as the crystallographic orientation of the parent grain. In practice, the normal vector $[\boldsymbol{H_C}, \boldsymbol{K_C}, \boldsymbol{L_C}]^{\boldsymbol{T}}$ of any possible twin plane in the crystal lattice coordinate system was transformed into the laboratory coordinate system by the following equation

$$\begin{bmatrix} \boldsymbol{H_L} \\ \boldsymbol{K_L} \\ \boldsymbol{L_L} \end{bmatrix} = \boldsymbol{G} \begin{bmatrix} \sqrt{3}/2 & 0 & 0 \\ -1/2 & 1 & 0 \\ 0 & 0 & \boldsymbol{c}/\boldsymbol{a} \end{bmatrix} \begin{bmatrix} \boldsymbol{H_C} \\ \boldsymbol{K_C} \\ \boldsymbol{L_C} \end{bmatrix}, \tag{9}$$

where $[\boldsymbol{H_L}, \boldsymbol{K_L}, \boldsymbol{L_L}]^{\boldsymbol{T}}$ is the normal vector of the twin plane in laboratory coordinate system, $\boldsymbol{a}$ and $\boldsymbol{c}$ are the lattice constants of Ti, and $\boldsymbol{G}$ is the transformation matrix determined by the Euler angles of the parent grain:

$$G = \begin{bmatrix} \cos\varphi_1\cos\varphi_2 - \sin\varphi_1\sin\varphi_2\cos\Phi & \sin\varphi_1\cos\varphi_2 + \cos\varphi_1\sin\varphi_2\cos\Phi & \sin\varphi_2\sin\Phi \\ -\cos\varphi_1\sin\varphi_2 - \sin\varphi_1\cos\varphi_2\cos\Phi & -\sin\varphi_1\sin\varphi_2 + \cos\varphi_1\cos\varphi_2\cos\Phi & \cos\varphi_2\sin\Phi \\ \sin\varphi_1\sin\Phi & -\cos\varphi_1\sin\Phi & \cos\Phi \end{bmatrix} \tag{10}$$

where $\boldsymbol{\varphi}_1$, $\boldsymbol{\Phi}$ and $\boldsymbol{\varphi}_2$ are the Euler angles output from the Aztec software.

Then, the angle β_{cal}, between the x-axis of the laboratory coordinate system and the calculated trace of the twin plane was readily computed by

$$\boldsymbol{\beta}_{cal} = \arctan(-\boldsymbol{H}_L / \boldsymbol{K}_L). \tag{11}$$

For each grain, all the six reported twin modes, namely $\{11\overline{2}2\}\langle 11\overline{2}3\rangle$, $\{10\overline{1}2\}\langle\overline{1}011\rangle$, $\{11\overline{2}1\}\langle\overline{1}\overline{1}26\rangle$, $\{11\overline{2}3\}\langle 11\overline{2}\overline{2}\rangle$, $\{11\overline{2}4\}\langle 22\overline{4}\overline{3}\rangle$, and $\{10\overline{1}1\}\langle\overline{1}012\rangle$, as well as the crystallographic symmetry of hexagonal close-packed metals, were considered and thus 36 β_{cal} were generated. The smallest misorientation angle and its corresponding axis of each twin mode was listed in Table 2. Then, the experimentally measured angle β_{exp}, between the x-axis of the laboratory coordinate system and a certain detected line was compared with all these 36 β_{cal} and sequenced in the ascending order. If the best match is within a prescribed tolerance, the detected line was considered to be the trace of a twin plane. The tolerance, which depends on the thermomechanical history and local plastic deformation of the specimen as well as the orientation measurement accuracy, was set to be $\pm 4^o$ semi-empirically. In this way, some detected line segments were excluded, resulting in the detected twin boundary map in Fig. 4(f).

In Fig. 4(f), all the twin boundaries identified using the automatic method introduced above were plotted in solid lines. In general, most of them are accurately identified, while mistakes were not completely avoided due to the noise. A few detected twin boundaries were actually false ones according to the perceptional comparison with Fig. 4(c), which were highlighted in the yellow color. Some of the twin boundaries such as the ones at the bottom right corner were not picked, and some parts, especially close to the ends, of the twin boundaries were missing, such as the ones at center left. All the missing twin boundaries in this grain were marked with dashed green lines. Quantitatively, the length of all the false boundaries was about 7% of the correctly detected ones, while the missing ones were about 12% of the total twin boundaries. Similar procedure was performed on 10 grains. While the ratios varied from grain to grain, all of them are around 10%. The twin boundary identification can be more accurately performed by checking the characteristic bands in the Kikuchi patterns recorded in the regions of disputed segments. However, the algorithm needs to be refined to make this process reliable and time efficient.

The comparison between the theoretically calculated β_{cal} of all the 36 possible twin modes and the experimentally measured β_{exp} not only filtered the mistaken features of the twin traces, but also offered a viable route to characterize the twin mode. However, the grain in Fig. 4 was not an ideal candidate to cross-check whether the twin mode was correctly identified in this manner since the Kikuchi patterns taken on this grain were poorly indexed when a commercial software is utilized. Consequently, another grain displayed in Fig. 5(a) was taken as an example, in which the Kikuchi patterns from the twin lamellae were partially indexed. The twin boundaries, including their spatial distribution and twin modes, were characterized based on the orientation map by looking up the table illustrated earlier in (Li et al., 2015). The grain boundary map, displayed in Fig. 5(b), suggests that the twin mode in this grain is $\{11\overline{2}2\}\langle 11\overline{2}3\rangle$. Careful examination indicated that the green and cyan colored spots in this map, corresponding to $\{10\overline{1}2\}\langle\overline{1}011\rangle$ and $\{10\overline{1}1\}\langle\overline{1}012\rangle$ twin modes respectively, were caused by the mis-indexed orientations output from the Aztec software. Also, because of the low indexing ratio, the twin boundaries appear broken in the map, which could lead to inaccurate estimation of the twin boundary fraction. Keeping this in mind, the twin boundary traces were delineated using the EBSD band contrast map data mining method that was introduced earlier. Here, the twin types were labelled in the same color scheme. From Fig. 5(c), a total of 46 twin boundary traces were noted in this grain. For further detailed analysis, all the detected twin boundaries were sequenced by their length in a descending order. With the new approach, continuous lines and instead of discrete spots were identified as twin boundary traces. 34 out of the total 46 twins were characterized as $\{11\overline{2}2\}\langle 11\overline{2}3\rangle$ type, consistent with the traditional method, while the twin type identified for the other 12 traces, whose sequence was marked in Fig. 5(c), were probably inaccurate. It was observed that most of these are twins with relatively shorter length (with the order ranging from No. 23 to No. 46). Quantitative measurements revealed that the total detected twin boundary traces in this grain were 925 μm long, and 22% of them (200 μm) were assigned with the incorrect twin type. All these unsuccessfully characterized twin modes were summarized in Table 3. Because the angular deviations between the detected lines and the calculated $\{11\overline{2}2\}\langle 11\overline{2}3\rangle$ variant were reasonably small, while the best match were still closer to the experimental results, it was concluded that the difficulty of twin type characterization came from two major reasons. First, the trace line detection was inaccurate, which was influenced by the contrast of the EBSD band map, as well as the plastic deformation even after twin formation. Second, all

Table 2
The misorientation angle/axis of tension and compression twin systems in Ti (Bisht et al., 2018).

Twin mode	System	Misorientation angle/axis
Tension twin 1	$\{10\overline{1}2\}\langle\overline{1}011 >$	85.49^o along$< 11\overline{2}0 >$
Tension twin 2	$\{11\overline{2}1\}\langle\overline{1}\overline{1}26 >$	34.69^o along $< \overline{1}010 >$
Tension twin 3	$\{11\overline{2}3\}\langle\overline{1}\overline{1}22 >$	$86.27\ ^o$ along $< \overline{1}010 >$
Compression twin 1	$\{11\overline{2}2\}\langle 11\overline{2}\overline{3} >$	63.98^o along $< \overline{1}010 >$
Compression twin 2	$\{10\overline{1}1\}\langle\overline{1}012 >$	56.82^o along $< 11\overline{2}0 >$
Compression twin 3	$\{11\overline{2}4\}\langle 22\overline{4}\overline{3} >$	77.35^o along $< \overline{1}010 >$

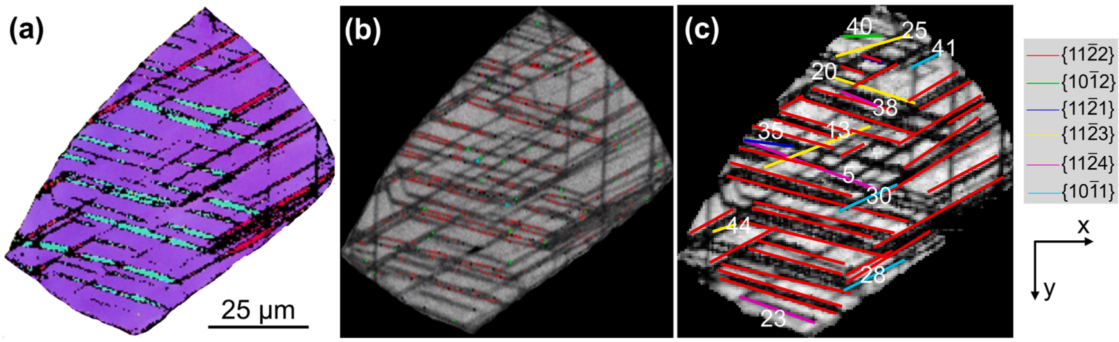

Fig. 5. The characterization of the twin types. From the IPF along the *x*-axis (a), twin boundaries, as colorful discrete spots, were calculated and superposed with the band contrast map (b). The twin boundaries were also identified with the novel line detection method and labelled with colors according to the twin type (c).

Table 3
The summary of the incorrectly characterized twin types.

Length order	β_{exp}	β_{cal1} for $11\bar{2}2$	$\lvert\beta_{exp} - \beta_{cal1}\rvert$	Best match (β_{cal2})	$\lvert\beta_{exp} - \beta_{cal2}\rvert$
5	20.4°	16.1°	4.3°	19.7° for {11$\bar{2}$4}	0.7°
13	158.7°	151.3°	7.4°	158.5° for {11$\bar{2}$3}	0.2°
20	17.5°	16.1°	1.4°	18.5° for {11$\bar{2}$3}	1.0°
23	19.2°	16.1°	3.1°	19.7° for {11$\bar{2}$4}	0.5°
25	163.9°	151.3°	12.6°	162.4° for {11$\bar{2}$3}	1.5°
28	153.2°	151.3°	1.9°	154.7° for {10$\bar{1}$1}	1.5°
30	155.5°	151.3°	4.2°	154.7° for {10$\bar{1}$1}	0.8°
35	7.3°	16.1°	8.8°	8.0° for {11$\bar{2}$1}	0.7°
38	21.5°	16.1°	5.4°	19.7° for {11$\bar{2}$4}	1.8°
40	179.5°	16.1°	16.6°	174.7° for {10$\bar{1}$2}	4.8°
41	153.4°	151.3°	2.1°	154.7° for {10$\bar{1}$1}	1.3°
44	162.5°	151.3°	11.2°	162.4° for {11$\bar{2}$3}	0.1°

the possible 36 twin planes resulted in 36 traces, and thus they were distributed rather densely in an angular space (The angular space could be considered as a 1D space with orientations ranging from 0 to π). The method based on the misorientation calculation between adjacent pixels in the orientation map is more reliable because both misorientation angle and axis were counted. The angle-axis space could be regarded as a 3D space. Hence, the 36 possible twin types distributed in the 3D space sparsely. Combined effects of these two led to the relatively high failure probability of the twin type characterization.

Briefly, with the newly developed EBSD data mining strategy, namely the band contrast map based method, the twin densities could be measured with a relatively smaller error of about 10%, while the twin type characterization was less successful, with an accuracy of about 80%. Therefore, in this study, we employed this approach to study the twin density evolution as a function of depth along the laser shock propagation direction, while the characterization of twin types still relied on the traditional method, namely the crystal orientation map based method.

The fraction of twin boundaries (TBs) in each individual grain was quantified as:

$$F_{TB} = \frac{\text{total pixels of verified TBs}}{\text{total pixels of verified TBs} + \text{the total pixels of grain boundaries}} \tag{12}$$

In this study, the average twin boundary fraction of all grains (all more than 20 grains) in each EBSD scanned area was estimated and compared.

3. Results

3.1. Surface microstructure after one LSP impact

To investigate the deformation mechanisms in Ti after the LSP treatment, the cross-sectional microstructures from the top surface to ~800 μm deep in the specimen subjected to a single LSP impact are characterized using EBSD. In Fig. 6(a), a 900 (TD) × 300 (ND) μm^2 area at the shocked edge on the cross-sectional plane is displayed. The black area at the bottom of the map indicates the edge of the specimen. Through the statistical analysis of the twin boundaries in more than 20 grains using the band contrast map based method, the average proportion of the twin boundaries in this region is estimated to be 79%. The twin boundary and band contrast maps are superposed in Fig. 6(b), which displays complex twin structures and multiple twin types inside the grains. From the misorientation

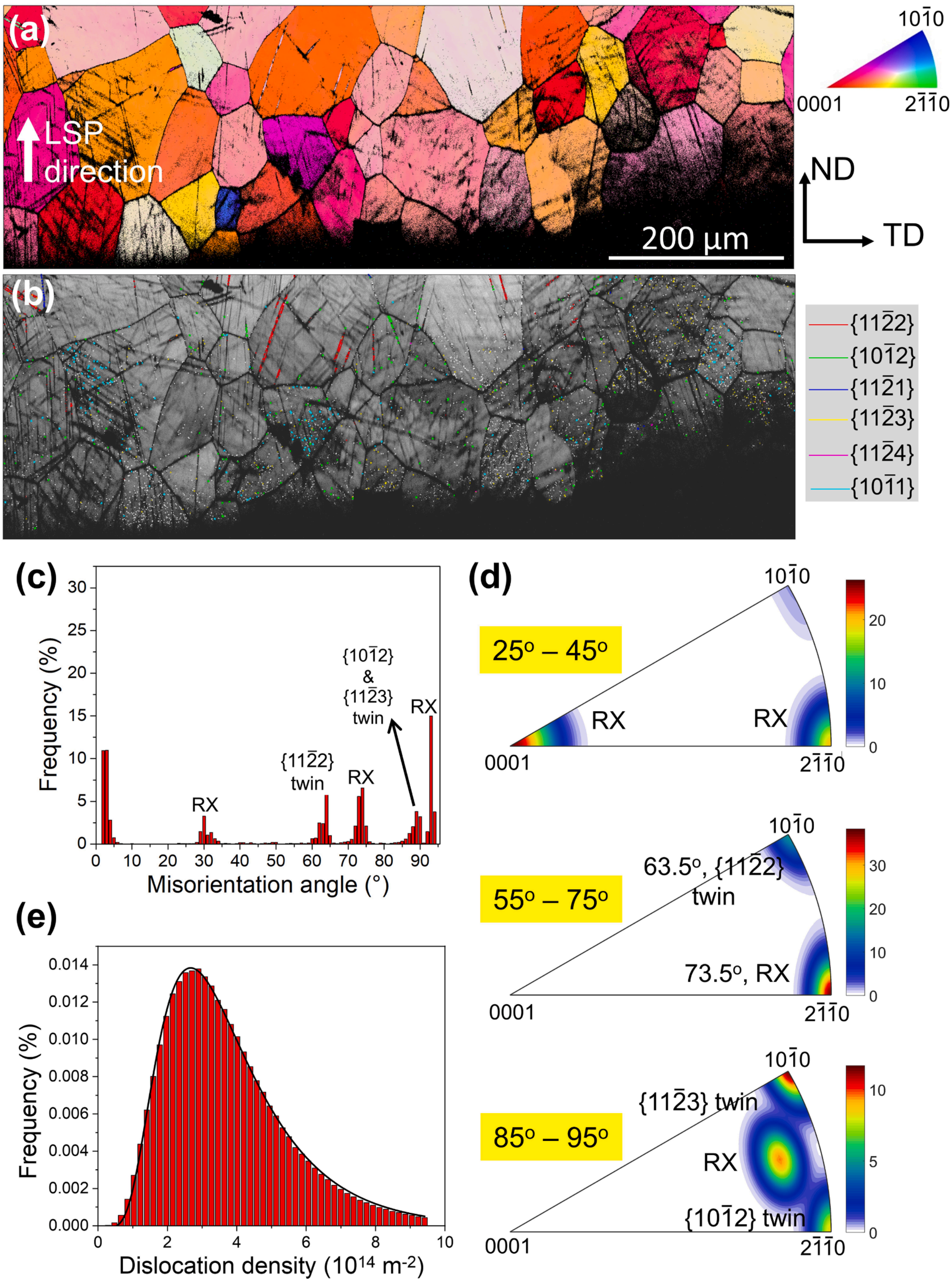

Fig. 6. Microstructure of the specimen surface subjected to 1 LSP impact. The EBSD IPF (a) along ND and twin boundary superposed band contrast map (b) show complex twin structures. The misorientation angle distribution histogram (c), inverse pole figures (d) suggest both twinning and dynamic recrystallization (RX). High density of geometrically necessary dislocations (GNDs) are also produced (e).

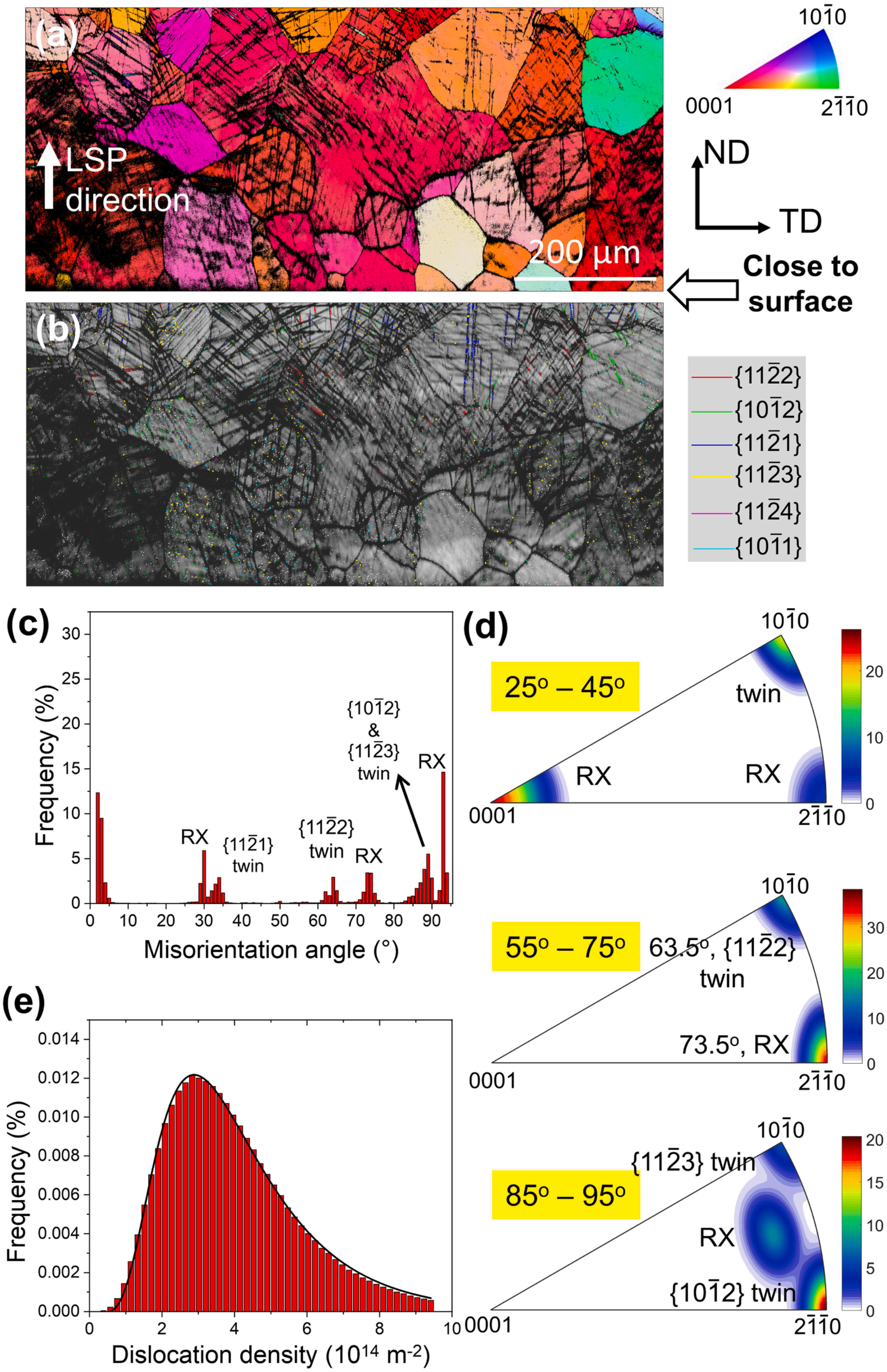

Fig. 7. Surface microstructure of the specimen subjected to 3 LSP impacts: (a) EBSD inverse pole figure map along ND, (b) band contrast map superposed with twin boundaries, (c) misorientation angle histogram, (d) inverse pole figure of various misorientation angle ranges, and (e) dislocation density histogram.

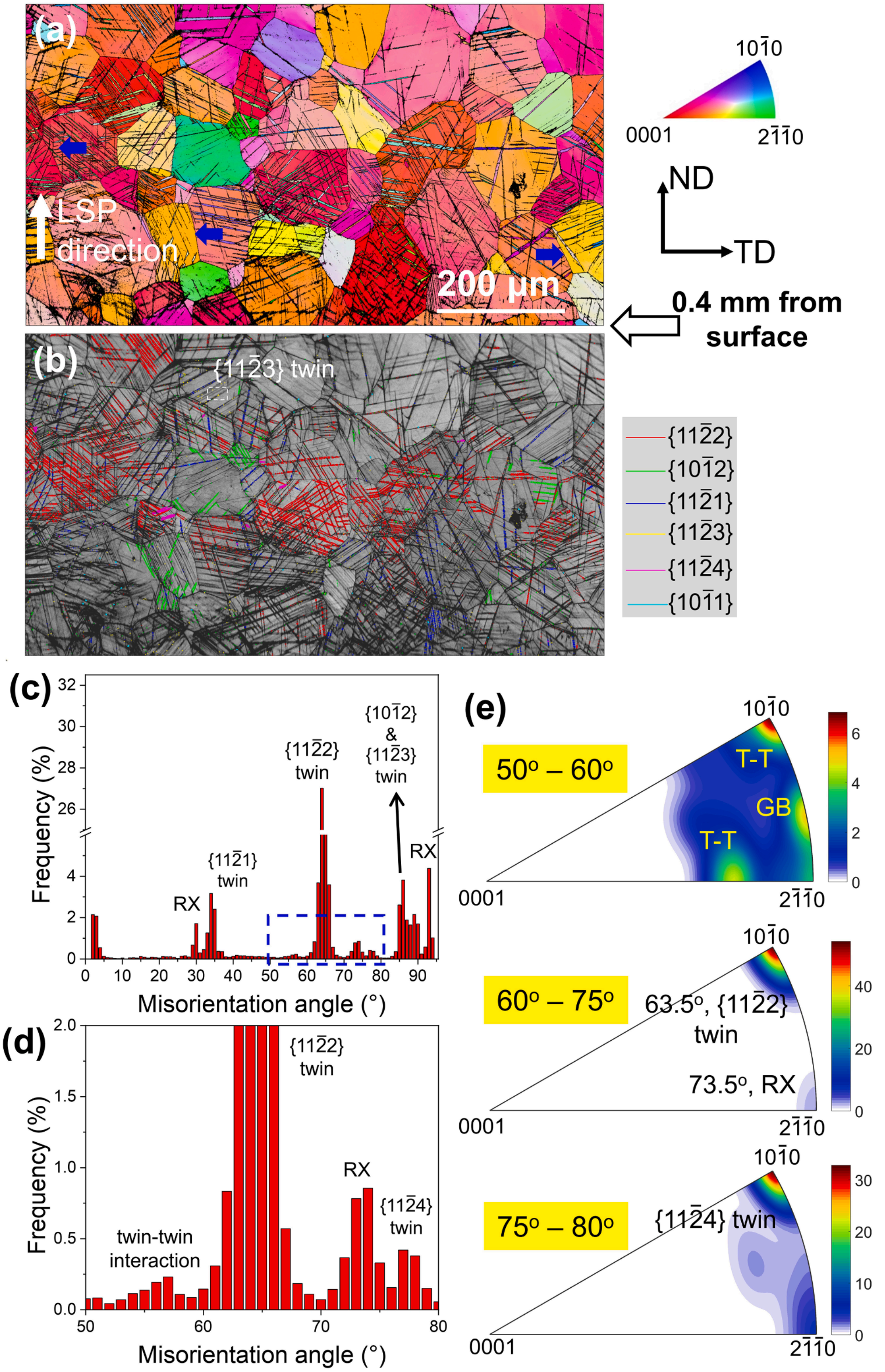

Fig. 8. Microstructures in the region 400 μm below the laser shock peened surface of the specimen subjected to 3 LSP impacts: (a) inverse pole figure map along ND, (b) band contrast map superposed by twin boundaries, and (c) misorientation angle histogram. Misorientation from 50° to 80° is studied in detail, with the histogram (d) and inverse pole figures (e) plotted.

angle distribution histogram shown Fig. 6(c), several peaks are observed, which occur at approximately 30°, 64°, 74°, 89°, and 93°. To understand their formation mechanism, their misorientation axes need to be taken into consideration. IPF maps in three different angular ranges are displayed in Fig. 6(d). Misorientations of about 29.5° and 32.5° were observed along the $\langle 0001\rangle$ and $\langle 2\overline{11}0\rangle$ axes, respectively, both of which are typical dynamic recrystallization features in Ti alloys (Zhao et al., 2019). Around $\langle 10\bar{1}0\rangle$, relatively fewer misorientation angles of 33.5° were observed. They indicate a low density of $\{11\bar{2}1\}\langle\overline{11}26\rangle$ twins. In the IPF map for 55 – 75°, a misorientation at 63.5° around $\langle 10\bar{1}0\rangle$ is observed. It corresponds to the formation of $\{11\bar{2}2\}\langle 11\bar{2}\bar{3}\rangle$ twin, while the 73.5° misorientation observed along $\langle 2\overline{11}0\rangle$ indicates dynamic recrystallization. Finally, the two misorientations at 89.5°, along $\langle 10\bar{1}0\rangle$ and $\langle 2\overline{11}0\rangle$ suggest the existence of $\{11\bar{2}3\}\langle 11\overline{22}\rangle$ and $\{10\bar{1}2\}\langle\bar{1}011\rangle$ twins, respectively. The misorientation at an even higher angle, observed at 93.5° along the $(\bar{9}\ 12\ \bar{3}\ 5)$ plane normal, is probably due to dynamic recrystallization, although it deviates slightly (~8°) from that reported in literature (Zhao et al., 2019). Additionally, the densities of geometrically necessary dislocations (GNDs) are computed and mapped by measuring the misorientation angles between each pair of adjacent pixels (Pantleon, 2008). The magnitudes of GND densities are displayed in the histogram of Fig. 6(e). By fitting the distribution using the log-normal function, the average dislocation density in this region is determined to be $(3.9 \pm 2.1) \times 10^{14}\ m^{-2}$. This result suggests that both dislocations and twins play an important role in the plastic deformation of Ti in the region close to the surface after 1 LSP impact. The distributions of the twin boundary and GND densities in the depth range of 300 – 800 μm are also quantified and summarized. They will be used in the discussion on the strengthening mechanisms (Section 4.3).

3.2. Gradient microstructures along the depth after 3 impacts of LSP

For the specimen subjected to three LSP impacts, three regions, one at the peened edge, second one at a depth of 400 μm, and the final one at a depth of 1.6 mm from the peened edge, were investigated.

A $900 \times 400\ \mu m^2$ area at the shocked edge on the cross-sectional plane is displayed in Fig. 7(a). Compared to the twin boundary map of the specimen subjected to one LSP impact, significantly more complex twin structures are observed in the peened surface after multiple impacts, as shown in Fig. 7(b). Peaks are found in the misorientation histogram (Fig. 7(c)) at similar positions as that in the specimen after 1 impact, but with different relative heights. The following significant differences are observed in IPFs (Fig. 7(d)). (i) A much stronger peak is found at 33.5° along $\langle 10\bar{1}0\rangle$, implying the increase of the $\{11\bar{2}1\}\langle\overline{11}26\rangle$ twin density. (ii) The intensity of the misorientation peak at 84.5° along $\langle 2\overline{11}0\rangle$ increased dramatically relative to the other peaks. This observation indicates that a higher density of $\{10\bar{1}2\}\langle\bar{1}011\rangle$ twins are introduced with more impacts of LSP than the other twin types. Quantitative analysis of twin densities by the band contrast map data mining approach indicates that the total twin boundary fraction of this region is about 80%, and the GND density is $(4.2 \pm 2.3) \times 10^{14}\ m^{-2}$. Essentially, while the densities of both twins and dislocations after 3 LSP impacts are similar to those after 1 impact, the relative density of each twin type varies significantly.

An EBSD micrograph of 900 (TD) × 500 (ND) μm^2 is displayed in Fig. 8(a). The bottom edge of it is about 0.4 mm away from the peened surface. From the band contrast map (Fig. 8(b)), even more twins are observed in the sub-surface region compared to the surface area. By applying the data mining method, the twin boundary proportion is found to be 86%. From the twin boundaries observed in Fig. 8(b) and the misorientation histogram displayed in Fig. 8(c) and (d), $\{11\bar{2}2\}\langle 11\bar{2}\bar{3}\rangle$, $\{10\bar{1}2\}\langle\bar{1}011\rangle$, $\{11\bar{2}1\}\langle\overline{11}26\rangle$, $\{11\bar{2}4\}\langle 22\overline{43}\rangle$, and $\{11\bar{2}3\}\langle 11\overline{22}\rangle$ twins were noted. They are similar to what has been observed in the region at the shocked edge. A significant increase in the density of the $\{11\bar{2}2\}\langle 11\bar{2}\bar{3}\rangle$ twins is also noted, leading to a commensurate increase in the misorientation peak at 63.5°. A detailed analysis of the misorientation angle distribution between 50° to 80°, using both the histogram displayed in Fig. 8(d) and the IPF maps in Fig. 8(e), suggests new twinning types and structures. The 76.5° misorientation along $\langle 10\bar{1}0\rangle$ comes from

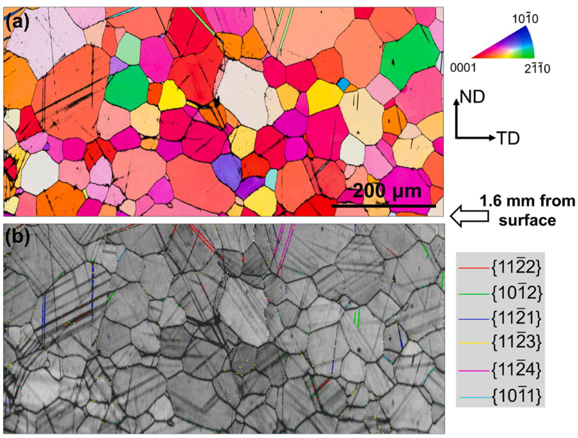

Fig. 9. Microstructures at a depth of 1.6 mm inside the peened surface in the specimen subjected to 3 LSP impacts: (a) EBSD inverse pole figure map along ND, (b) band contrast map with twin boundaries.

the $\{11\overline{2}4\}\langle 22\overline{4}\overline{3}\rangle$ twin boundaries, which is not observed in other regions and rarely reported in the literature on LSP treated Ti. The misorientation angles of about 50.5° along $\langle 10\overline{1}0\rangle$ and 56.5° along the $(4\overline{2}\overline{2}3)$ plane normal are consistent with the intersections between two different pairs of variants of $\{11\overline{2}2\}\langle 11\overline{2}3\rangle$ twins (marked as T-T in the first inverse pole figure). In other words, a high density of several variants of $\{11\overline{2}2\}\langle 11\overline{2}3\rangle$ twins are active in this region, resulting in various types of boundaries with different misorientation angles and axes. In addition to these, this region also contains grain boundaries with ~55° misorientation along the $(3\overline{1}\overline{2}0)$ plane normal, which are marked by blue arrows in Fig. 8(a). Similar features have hitherto not been reported in literature. For the sake of simplicity, we marked them as GBs (grain boundaries) in the IPF map (see Fig. 8(e)). The GND density measured in this region is $(3.1 \pm 1.6) \times 10^{14}$ m^{-2}, lower than that in the peened surface.

Finally, an area of 836 × 400 μm^2 on the TD-ND plane at a depth of 1.6 mm from the peened surface is investigated. The EBSD IPF map along the ND is depicted in Fig. 9(a). Although this region is far away from the peened surface, the intersectional traces in Fig. 9(b) shows that twin boundaries are still formed. Adopting the hitherto employed approach that combines misorientation distribution histogram and IPF maps, the twin types are identified as $\{11\overline{2}2\}\langle 11\overline{2}3\rangle$, $\{11\overline{2}1\}\langle\overline{1}\overline{1}26\rangle$, $\{10\overline{1}2\}\langle\overline{1}011\rangle$, $\{11\overline{2}3\}\langle 11\overline{2}\overline{2}\rangle$, and $\{11\overline{2}4\}\langle 22\overline{4}\overline{3}\rangle$. Quantitative analysis indicates that the proportion of twin boundaries is 69%, and the dislocation density is $(2.8 \pm 1.4) \times 10^{14}$ m^{-2}, both of which are significantly lower than that in the other two regions.

3.3. Microhardness gradients

The variations in the microhardness as a function of depth along the laser shock propagation direction in the specimens subjected to 1 and 3 LSP impacts are displayed in Fig. 10. For reference, the micro-hardness data of the fully annealed specimen is also included. The average hardness of the fully annealed specimen is ~138 HV, which remains the same at every location along the depth, within a reasonable margin of error. In both the LSP treated specimens, the microhardness decreases monotonically, barring a few fluctuations, with increasing depth. Eventually, at a depth of 1500 - 1600 μm from the surface, in both the specimens, hardness plateaus at ~140 HV, comparable to that of the annealed specimen. This suggests that the effective peening depth is ~1.6 mm, which is similar to that reported in the LSP treated Ni-based superalloys (Zhou et al., 2022), irrespective of the number of LSP impacts the material is subjected to. The microhardness increases dramatically to 192 HV at the peened surface of the specimen with 3 LSP impacts, while the maximum microhardness of the specimen peened with 1 LSP impact is 175 HV. The remarkable hardening effect originates from the microstructural changes induced by LSP at ultra-high strain rates, which will be discussed later.

4. Discussion

The novel EBSD band contrast map analysis strategy developed in this study enabled an effective identification of the twin boundaries over large sampling areas. The observations provide a direct experimental evidence that high densities and various types of twins are generated in a depth range of millimeter scale. The twin-twin and twin-dislocation interactions, the deformation and subdivision mechanisms, and their contributions to the strengthening are discussed in detail in the following.

4.1. Interactions of twins and dislocations

Five different twin types are detected in the LSP affected zone examined in this work. They are $\{11\overline{2}2\}\langle 11\overline{2}3\rangle$, $\{10\overline{1}2\}\langle\overline{1}011\rangle$, $\{11\overline{2}1\}\langle\overline{1}\overline{1}26\rangle$, $\{11\overline{2}3\}\langle 11\overline{2}\overline{2}\rangle$, and $\{11\overline{2}4\}\langle 22\overline{4}\overline{3}\rangle$. Although prior research also reported LSP-induced mechanical twins in Ti and Ti alloys, multiple twin types in a single specimen are identified for the first time in this study. Amongst them, the $\{11\overline{2}2\}$ and $\{10\overline{1}2\}$ twins are easier to form and hence most frequently observed (Ghaderi and Barnett, 2011; Bao et al., 2013; Qin and Jonas, 2014) as they

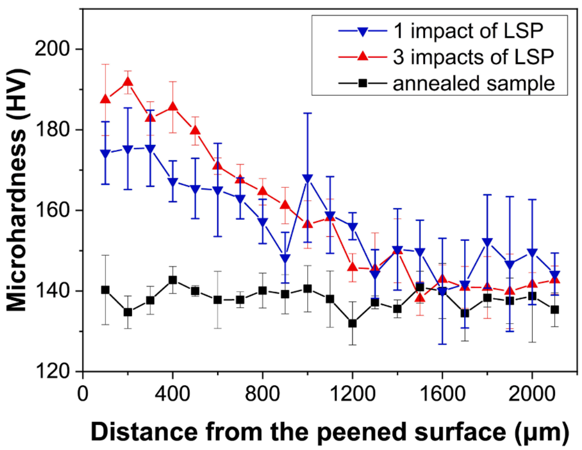

Fig. 10. Microhardness gradient along the depth from the peened surface to the interior.

possess a small shuffling parameter and low twin shear (Chun et al., 2005), respectively. Similarly, the formation of the $\{11\bar{2}1\}$ twin also involves simple atomic shuffles and are thus easily induced by the plastic deformation in Ti (Chichili et al., 1998). Aside these three, the $\{11\bar{2}4\}$ twins are observed almost exclusively in Ti subjected to deformation at high strain rates (Xu et al., 2012; Lainé and Knowles, 2015). Since the strain rate during LSP can reach up to 10^6 s^{-1} (Zhou et al., 2013), the observation of $\{11\bar{2}4\}$ twins in the peened layers is not surprising. However, observation of the $\{11\bar{2}3\}$ twins were rarely reported in literature and more investigations are needed to understand their origin.

Various types of twins and their different variants formed in the Ti grains, result in numerous twin-twin intersections and introduce grain boundary misorientations. The grain boundary map of different misorientation angles in the region 400 μm away from the peened surface in the sample subjected to 3 LSP impacts is depicted in Fig. 11(a). Five regions, marked from b to f, are magnified and scrutinized individually. Six $\{11\bar{2}2\}$ twin variants are observed in the grain shown in Fig. 11(b). By assuming that the direction of compressive stress is parallel to the LSP direction, the Schmid factor of each twin variant is calculated and listed in Table 4. It is well accepted that the twin variants with the Schmid factors greater than 0.3 are easily activated (Jonas et al., 2011). Thus, data shown in Table 4, provides a rationale as to why $(1\bar{2}1\bar{2})$, $(11\bar{2}2)$, $(2\bar{1}\bar{1}2)$ and $(2\bar{1}\bar{1}\bar{2})$ twins are observed in the grain. The $(1\bar{2}12)$ and $(11\bar{2}\bar{2})$ twin variants, the Schmid factor of which are less than 0.3 are also observed, indicating that the local stress direction is probably deviated from the LSP direction because of the interactions among grain boundaries, twin boundaries, and dislocations.

The circled area, labeled 1, in Fig. 11(b) highlights the intersection of two $\{11\bar{2}2\}$ twin variants, resulting in the misorientations of 57.7° with the $(\bar{5}9\bar{4}6)$ plane normal. The theoretical misorientation angles/axes (plane normal) of various twin-twin intersections are calculated and listed in Table 5. Within a tolerance of 8°, the misorientation between the impinged twins is consistent with the theoretical misorientation angle/axis, which is at 60.0° to the $(\bar{2}4\bar{2}3)$ plane normal. In the misorientation map, another subgrain boundary, with the misorientation angle of 3.4° to the $(\bar{1}\ 1\ 0\ 12)$ plane normal with respect to the adjacent pixels, is detected. Although such low angle grain boundary is not directly formed by impingement of twins, it is believed to be generated in the processing of twin-twin intersections and the accompanying dislocation activity, resulting in a small rotation around the axis close to [0001]. Likewise, the high angle grain boundaries enclosed in Circles 2 to 4 in Fig. 11(c) to (e) are formed from the intersections between a pair of primary twins. Their misorientation angle/axis as well as twin-twin intersection types are all listed in

Due to the ultra-high strain rate deformation of the material during LSP, secondary twins are introduced in Ti. An example is highlighted by the Circle 5 in Fig. 11 (f), where secondary $\{10\bar{1}2\}$ tension twin variants nucleate and grow in the thick $\{11\bar{2}2\}$ primary compression twin lamellae. As the $\{10\bar{1}2\}$ twins grow through the thickness of the primary twins and eventually intersect with the

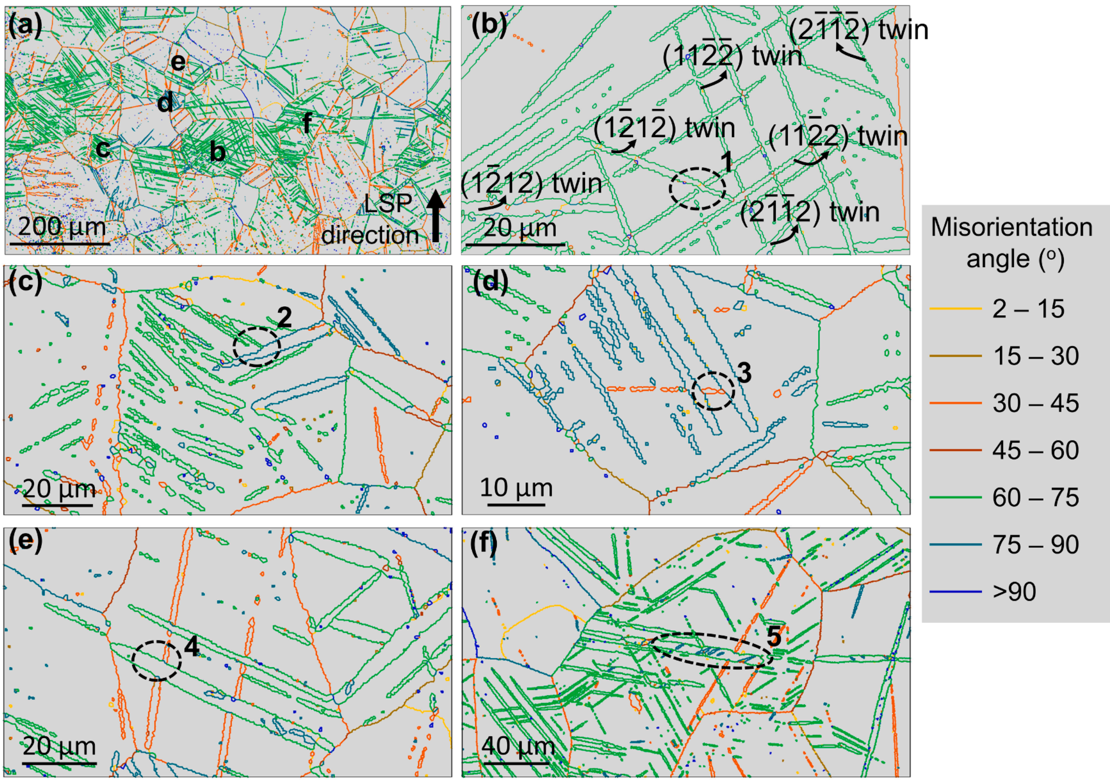

Fig. 11. Investigation of the twin-twin intersections in the sample subjected to 3 LSP impacts: high angle grain boundaries in a region (a) with high density of twins, (b - e) impinging twins, and (f) secondary twins.

Table 4
The Schmid factor of each twin variant in Fig. 11(b).

Twin variant	$(1\bar{2}1\bar{2})$	$(11\bar{2}2)$	$(2\bar{1}\bar{1}2)$	$(2\bar{1}\bar{1}\bar{2})$	$(1\bar{2}12)$	$(11\bar{2}\bar{2})$
Schmid factor	0.482	0.487	0.416	0.394	0.269	0.251

Table 5
The twin-twin intersection type and their misorientation angle/axis in Circle 1 to Circle 4 in Fig. 11

Region	Type	Misorientation angle/axis Experimental	Theoretical
Circle 1	$\{11\bar{2}2\}$ variants	57.7° along $(\bar{5}9\bar{4}6)$ normal	60.0° along $\{\bar{2}4\bar{2}3\}$ normal
Circle 2	$\{11\bar{2}2\}$ and $\{11\bar{2}4\}$ twins	69.6° along $(\bar{7}701)$ normal	70.4° along $\{\bar{6}601\}$ normal
Circle 3	$\{10\bar{1}2\}$ and$\{11\bar{2}1\}$ twins	57.5° along $(\bar{3}211)$ normal	66.5° along $\{\bar{2}3\bar{1}1\}$ normal
Circle 4	$\{11\bar{2}2\}$ and $\{11\bar{2}1\}$ twins	82.6° along $(\bar{1}100)$ normal	80.6° along $\{\bar{1}100\}$ normal

Table 6
Theoretical misorientations between the secondary twin and parent grain.

$\{10\bar{1}2\}$ secondary twin in $\{11\bar{2}2\}$ primary twin		
48.4° along $\{\bar{1}101\}$ normal	87.9° along $\{\bar{4}7\bar{3}0\}$ normal	41.4° along $\{\bar{4}5\bar{1}5\}$ normal

parent grain, grain boundaries with specific misorientation angle and axis are formed. All the possible misorientation angles/axes between the parent grain and the $\{10\bar{1}2\}$ secondary twins are listed in Table 6. From the EBSD results, a grain boundary oriented at 47.4° to the $(\bar{1}101)$ plane normal is found (highlighted by the Circle 5), which is at 48.4° to the $(\bar{1}101)$ normal theoretical misorientation and hence is within the permissible tolerance limits.

It is now worth asking why the $\{10\bar{1}2\}$ secondary tension twins are largely observed within the $\{11\bar{2}2\}$ primary compression twins. We believe that since the *c*-axis of the grains in the fully annealed specimen is relatively close to the LSP direction (about 30° off), $\{11\bar{2}2\}$ compression twins rather than the $\{10\bar{1}2\}$ tension twins are first formed under the compressive stress caused by the laser shock. The introduction of the $\{11\bar{2}2\}$ primary compression twins tilt the *c*-axis of the grain by ~64°, making it almost perpendicular to the LSP impact direction. In this condition, the laser shock stress resolved along the *c*-axis is tensile in nature and hence promotes the formation of $\{10\bar{1}2\}$ secondary tension twins within the $\{11\bar{2}2\}$ primary compression twins. In a prior study, secondary twins were also observed in laser shock peened Ti by the means of TEM (Lu et al., 2017), although their specific type and the high angle grain boundaries accompanying them, were not examined in detail.

To further understand the interaction between twins and dislocations, TEM investigations are conducted. The twins grow in a lamellar shape with widths of 100 to 500 nm near the shocked surface, as shown in Fig. 12(a) to (b). Abundant tangled dislocations are observed near the twin boundaries in the surface area as well as the regions 100 to 350 μm deep into the interior, as shown in Fig. 12(c) to (e). According to a prior study (Wang et al., 2014; Wang and Agnew, 2016; Sinha and Gurao, 2017; Ardeljan et al., 2017), the twin-twin intersections in Ti limit the available paths for the movement of dislocations and hence force the dislocations to pile up near the twin boundaries that are not impinged by other twins. The mutual interaction among dislocations and their interactions with the twin boundaries produces inhomogeneous internal stresses at the twin-twin junctions, which in turn, results in the deviation of the measured misorientation angle and direction from the theoretically predicted ones. It is noted that the dislocations in the parent grain become much more regular as the shock effect of the LSP treatment decays with increasing depth from the peened surface, as shown in Fig. 12(c) and (d). In the region 950 μm away from the surface, straight long dislocation lines are produced, probably due to the ultra-high strain rate and planar nature of the shock wave (Lainé et al., 2017). From these TEM analyses, it should be apparent that examining all the twin types and twin-twin interaction scenarios nearly-impossible because of the limited sampling area (although quite a few TEM specimens have been prepared and observed), highlighting the importance and necessity of developing the EBSD data mining approach.

4.2. Deformation mechanisms in pure Ti subjected to LSP

The quantitative estimates of dislocation densities and twin fractions at different depths in the specimen subjected to 3 LSP impacts is summarized in Table 7. The dislocation densities are measured using the following two methods: (i) the line-intercept method adopted by Norfleet et al. (2008) using the TEM images, and (ii) the Nye tensors based misorientation distribution (Pantleon, 2008) method using the EBSD scans. The preparation of TEM thin foils usually leads to stress relief leading to the escape of some dislocations. In contrast, EBSD detects GNDs but is incapable of detecting statistically stored dislocations. Therefore, the dislocation densities measured by either of the approaches is likely to be an underestimation. Nevertheless, both methods led to consistent results in the present study, showing that the dislocation densities decrease monotonically with the depth from the surface and eventually reach that of the undeformed material in both the samples subjected to 1 and 3 LSP impacts. The observation of a monotonic decrease of the

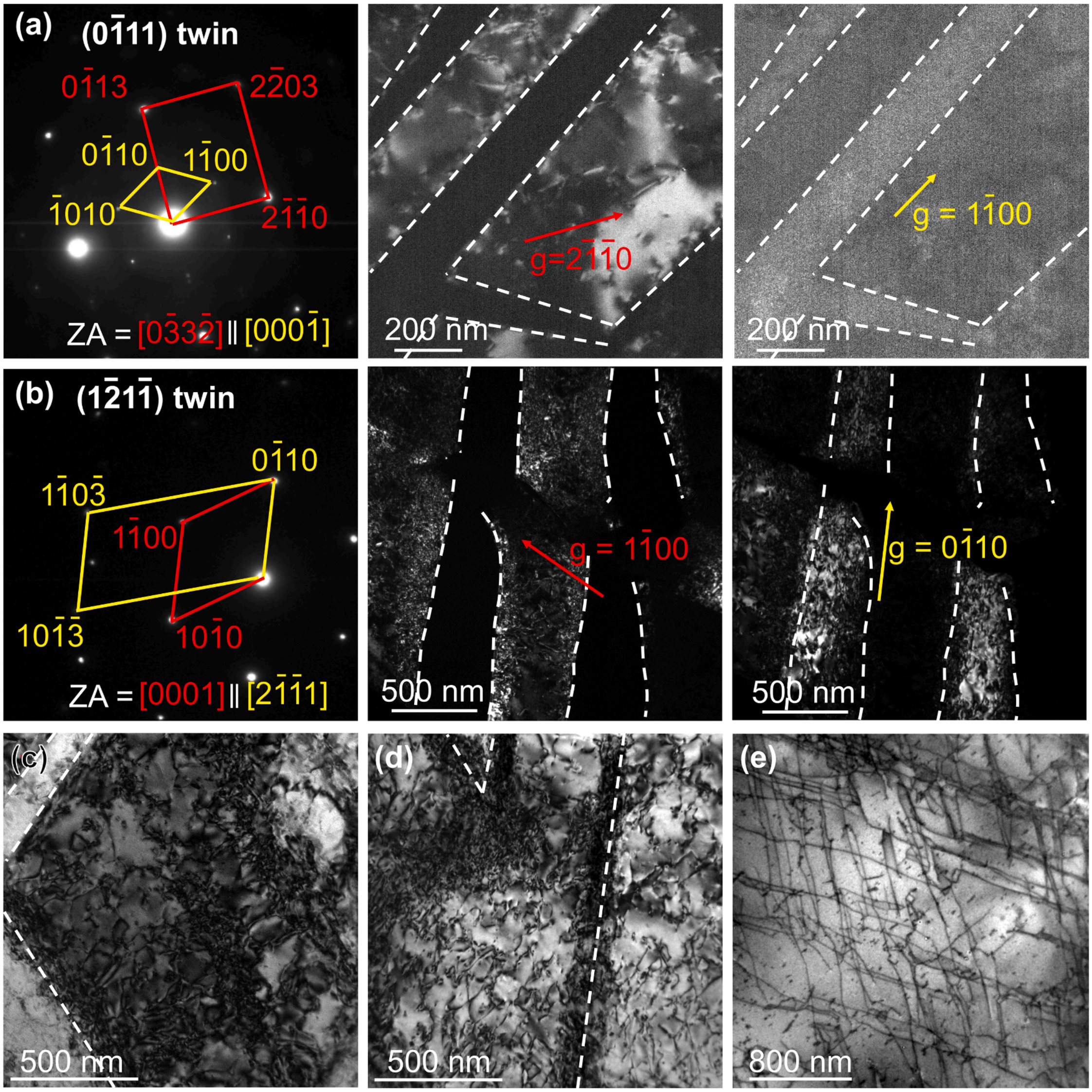

Fig. 12. TEM analysis of the specimen subjected to 3 LSP impacts. (a-b) show the selected area electron diffraction patterns as well as dark field images of the (01 ¯11) and (12 ¯11 ¯) twin structures in the region close to the surface; (c-e) demonstrate the dislocation structures about 100, 350 and 950 μm below the shocked surface, respectively. Dashed white lines indicate twin boundaries.

Table 7
The twin boundary fraction and dislocation density at various depths parallel to ND in the sample treated by 3 LSP impacts.

Position	Dislocation density ($\times$ 10^{14} m^{-2}) from TEM	from EBSD	Twin boundary fraction	Block size (μm)
Surface	5.1	4.2 ± 2.3	80%	8.5±1.2
400 μm deep	3.4	3.1 ± 1.6	89%	5.2±0.9
950 μm deep	2.1			
1.6 mm deep		2.8 ± 1.4	69%	12.4±3.7

dislocation density along the depth is likely a synergistic outcome of the following two effects. First, the strains caused by laser shock waves diminish along the depth (Lu et al., 2017; Yang et al., 2017). Second, LSP causes an increase in the temperature by a few hundred°C at the peened surface, which also drops with an increasing depth (Yang et al., 2017). According to a previous study (D'Yakonov et al., 2015; Dai and Song, 2022), the critical resolved shear stress for dislocation activation decreases as the temperature raises. Consequently, the combined effects of higher imposed strain and lower critical resolved shear stress manifests as higher dislocation densities in the grains at the surface of the LSP treated Ti metal.

Unlike the monotonic decrease in the dislocation density with increasing depth, observed in the specimen subjected to 3 LSP impacts, the proportion of twin boundaries increases from 80% at the surface to 86% at a depth of 400 μm from the peened surface, and then decreases to 69% in the region 1.6 mm away from the surface. A lower twin density at the surface was also observed in the specimen subjected to 1 LSP impact and mentioned in a prior study (Lainé et al., 2017; Yang et al., 2017). However, the present study unambiguously establishes that the twin density is relatively lower at the surface and only peaks at a depth of about 0.4 mm before gradually reducing. The non-monotonic variations in twin density along the depth is attributed to the following two factors. Unlike that seen for dislocations, the critical resolved shear stress for mechanical twins is insensitive to temperature (D'Yakonov et al., 2015). This implies that there is no specific driving force supporting the generation of a greater degree of twinning at the surface. Alternately, as mentioned above, more dislocations are activated at the surface by the synergistic effects of both mechanical stress and laser shock induced heat evolution. Considering that more plastic strain is accommodated by dislocations at the surfaces, the necessity of strain accommodation by twins is relatively lower. With increasing depth, a drop in dislocation density implies that twin formation is essential to accommodate a larger portion of the strain generated due to LSP.

On the basis of the detailed microstructural characterization performed in this work, the deformation mechanism of pure Ti subjected to multiple LSP impacts is schematically illustrated in Fig. 13. At the surface, the fraction of twin boundaries in the specimen subjected to 3 impacts of LSP is similar to that under 1 impact probably because the driving force for the activation of twinning remains almost the same after 1 and 3 LSP impacts at such ultra-high strain rates. With the increasing LSP impacts, strains accumulate, resulting in the induced twins becoming thicker. Consequently, at a given resolution in the EBSD experiments, relatively more twin boundaries are identified under 3 LSP impacts. To accommodate plastic deformation near the shocked surface, a high density of dislocations are generated by the shock wave. Due to the insufficient slip systems in Ti and the impedance of twin boundaries, dislocations cannot glide with ease, and those that are mobile get tangled, as displayed schematically in Fig. 13(a).

In the region 400 μm away from the peened surface, higher densities of twins are produced. In fact, even secondary twins are activated within the primary twins to accommodate the imposed strain. Therefore, intersections of different twin types and variants with each other become more frequent. All the primary and secondary twins, and twin-twin intersections result in boundaries with specific misorientations, subdividing the original Ti grains into numerous triangular or polygonal blocks, as illustrated in Fig. 13(b).

In regions far below the laser shock peened surface, a substantially diminished shockwave pressure limits the plastic deformation and culminates in the absence of substantial number of twins, as illustrated in Fig. 13(c), as well as regular arrays of long and planar dislocations.

4.3. Strength enhancement after LSP

The increased microhardness in the LSP treated specimen results from the subdivision of grains and multiplication of dislocations. Compared to the unpeened condition, the grains in the specimen subjected to LSP are subdivided into numerous triangular or polygonal blocks after 3 LSP impacts. The average block size distribution is measured from the EBSD band contrast maps and counted statistically at each 100 μm depth range (Fig. 14(a)). The average size of the subdivided blocks is about 9.5 and 8.5 μm at the peened edge subjected to 1 and 3 LSP impacts, respectively. Since the twin densities increases from the surface to the subsurface, the average subdivided block size also decreases. Similarly, the dislocation density is also studied statistically in each 100 μm depth range and displayed in Fig. 14(a). Barring that at the surface, a monotonic decrease in the dislocation density is observed from the surface to the interior. The relationship between the yield strength σ_y and dislocation density ρ and block size d is expressed by the following (Choi et al., 2021):

$$\boldsymbol{\sigma_y = \sigma_o + kd^{-1/2} + M\alpha Gb\rho^{1/2}}, \tag{13}$$

where $\boldsymbol{\sigma_o}$ is the yield strength of the dislocation-free coarse-grained specimen. The Hall-Petch coefficient, k, is ~300 MPa·$\boldsymbol{\mu m}^{1/2}$ (Hans and Conrad, 1981), d is the measured block size of the local material, Taylor factor, $M = 3$ (Choi et al., 2018), $\alpha = 0.33$ (Choi et al., 2018), shear modulus, G ~45GPa (Hans and Conrad, 1981), $b = 0.5515$ nm (Aubry et al., 2016) is the magnitude of the Burgers vector and $\boldsymbol{\rho}$ the measured local dislocation density.

According to the Tabor's empirical relation, σ_y equals to one third of the microhardness (Tabor, 1951). Therefore, the change in

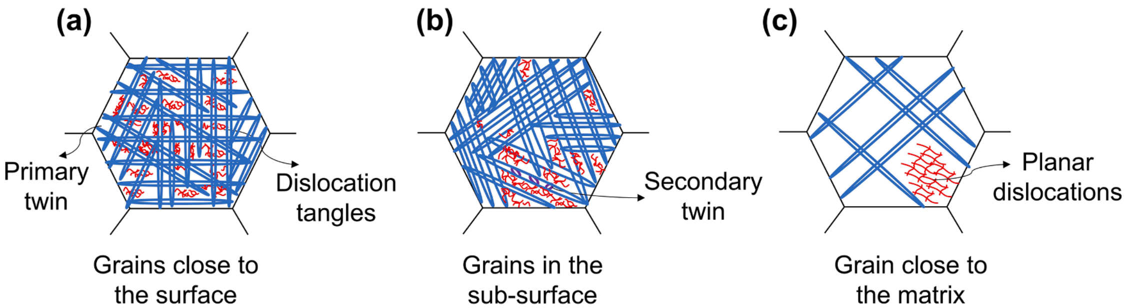

Fig. 13. Scheme of the deformation mechanism of pure Ti subjected to LSP impacts.

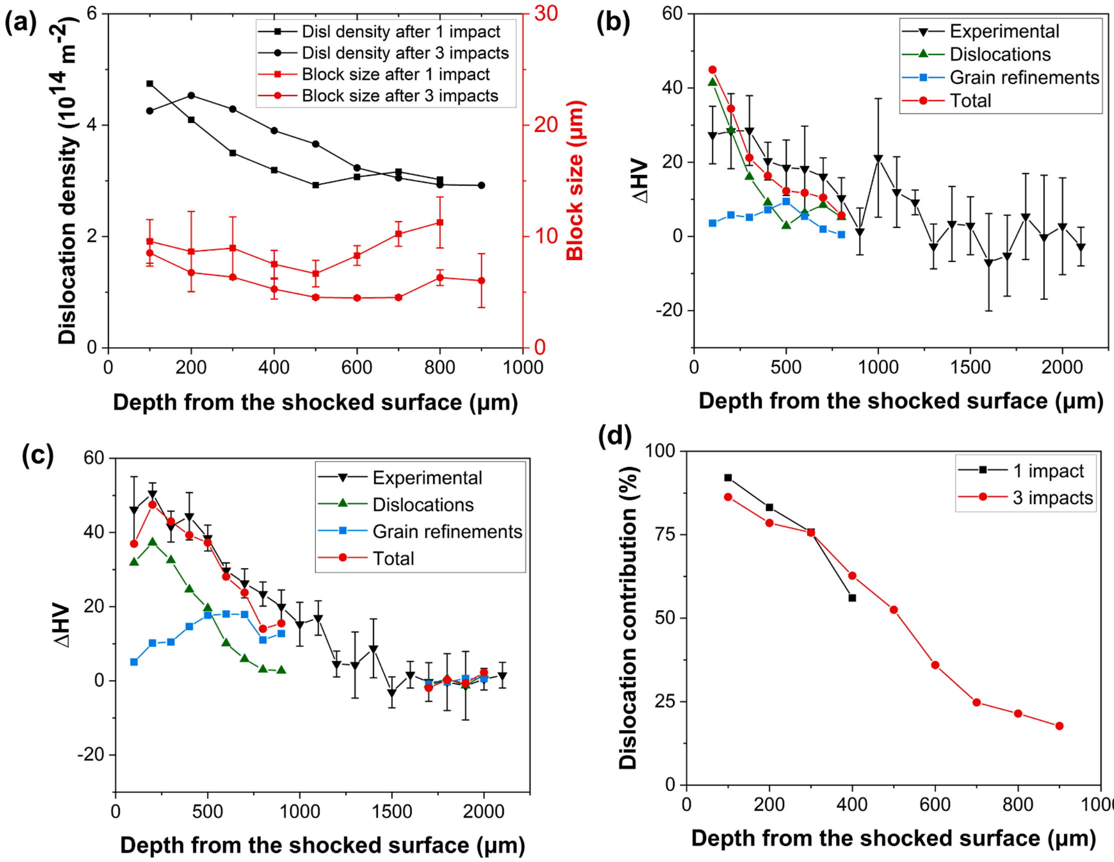

Fig. 14. Analysis of mcirohardness gradient along the depth. (a) shows the distributions of dislocation density and block size; (b) and (c) demonstrate the microhardness enhancements contributed from dislocations, grain refinements, and the summation of these two after 1 and 3 impacts, respectively; (d) displays the percentage of the microhardness increment caused by dislocations.

microhardness (ΔHV) at each depth relative to the matrix is estimated using the following equation (and in this manuscript we convert the microhardness from MPa to kgf·mm^{-2}):

$$\Delta HV = 3k \cdot \left(d^{-\frac{1}{2}} - d_{matrix}^{-\frac{1}{2}} \right) + 3M\alpha Gb \cdot \left(\rho^{\frac{1}{2}} - \rho_{matrix}^{\frac{1}{2}} \right). \tag{14}$$

In this study, we take the material at a distance > 1.6 mm away from the peened surface as the matrix.

On substituting the dislocation densities and block size measured from the EBSD data (Fig. 14(a)) into Eq. (14), the microhardness enhancement contributed from dislocations, grain refinements, and the summation of these two are plotted for LSP treated Ti with 1 and 3 impacts in Fig. 14(b) and 14(c), respectively. As a comparison, the experimentally measured ΔHV with respect to the hardness value of the base metal is also displayed. It is found that the calculated microhardness values based on the microstructural features agree reasonably with the experimental results, for both specimens after 1 and 3 impacts of LSP.

To quantify the relative contributions from dislocation-induced strengthening and the grain refinement effects, the fraction of ΔHV caused by dislocations is calculated (for the specimen with 1 LSP impact, only data from surface to 400 μm deep are included because the strengthening effect is week at deeper regions) for each location and then marked in Fig. 14(d). Interestingly, it is seen that for the first 400 μm, the contributions to ΔHV by dislocation-induced strengthening and grain refinement are similar for the two LSP treated specimens. Close to the surface, dislocations contribute to >90% of the ΔHV. With increasing depth from the peened surface, the contribution of dislocation-inducted strengthening to ΔHV decreases, and the strengthening via grain refinement becomes the primary mechanism. At the depth of about 500 μm, dislocations and grain refinements contribute equally to the strengthening and at the depth of 900 μm, three quarters of the ΔHV is contributed by refinement of the grains. The variations in the microhardness can also be explained by the variations in dislocation densities along the depth of the LSP treated specimens arising from LSP induced stresses and temperature rise at the surface.

The specimen with 1 and 3 LSP impacts have similar effective depths but show peak microhardnesses of 175 and 192 HV, respectively, at the peened surface. Since multiple LSP impacts provide longer time and more energy for deformation, the specimen with 3 LSP impacts induces more dislocations at the same depth, which rationalizes its greater microhardness compared to the specimen which was subjected to only 1 LSP impact.

5. Summary and Conclusions

The LSP induced microstructural gradients in Ti are examined in detail using EBSD in order to overcome the disadvantages of TEM, which is limited in terms of the probed volume and hence can be statistically insignificant. With the assistance of a custom designed EBSD data mining method, the fraction of twin boundaries is quantified for large area scans and multiple types of twins are identified. By detecting, merging, and verifying the straight lines in the band contrast maps of EBSD scans, twin boundaries are successfully identified. This approach is applicable to almost all EBSD band contrast maps and thus expected to be relevant for a wide range of materials. GND density is also calculated from the EBSD results, the trend of which agrees with the total dislocation density measured using TEM. Our study not only clarifies the gradient microstructural from the peened surface to the bulk interior, but also reveals the plastic deformation mechanisms along the depth in the laser shocked peened Ti. The microhardness and strengthening contributions of dislocations and twins, as well as their interactions that lead to grain subdivisions, are discussed. The important conclusions of this study are summarized as follows:

(1) Five twin types, namely $\{11\overline{2}2\}\langle 11\overline{2}3\rangle$, $\{10\overline{1}2\}\langle\overline{1}011\rangle$, $\{11\overline{2}1\}\langle\overline{1}\overline{1}26\rangle$, $\{11\overline{2}3\}\langle 11\overline{2}\overline{2}\rangle$, and $\{11\overline{2}4\}\langle 22\overline{4}\overline{3}\rangle$, were identified in Ti subjected to multiple LSP impacts. Among these, the last two types of twins are seldom reported. The results of this study provide clarifications for the contradictory observations made in the published literature regarding the formation of twin structures in metals and alloys subjected to LSP. Since previous studies utilized TEM to study twins, they could not sample a wider area and possibly observed only limited types of twins.
(2) The twin and dislocation density gradients are quantified at different locations from the peened surface to the interior of the specimen. Dislocation densities decrease monotonically with increasing depth, but the twin density initially increases and then monotonically decreases. Highest twin density is observed in the sub-surface area than at the surface, probably due to the balance of stresses and thermal effects.
(3) The misorientation angles and axes are studied in detail for the individual primary twin boundaries, their intersections between each pair of primary twins, and that between primary and secondary twin pairs. These boundaries subdivide the Ti grains into numerous sub-grains with specific misorientations. Since the twin boundaries impede the movement of dislocations, dislocations pile up near twin boundaries and lead to the development of an inhomogeneous stress field, which in turn manifests as a deviation in the measured misorientations from that of the theoretically predicted misorientations.

CRediT authorship contribution statement

Xuan Huang: Investigation, Visualization, Data curation. **Wenxin Zhu:** Formal analysis, Visualization. **Kai Chen:** Methodology, Supervision, Writing – original draft. **R. Lakshmi Narayan:** Writing – review & editing. **Upadrasta Ramamurty:** Writing – review & editing. **Liucheng Zhou:** Conceptualization, Supervision, Funding acquisition. **Weifeng He:** Project administration, Resources.

Declaration of Competing Interest

The authors declare that they have no known competing financial interests or personal relationships that could have appeared to influence the work reported in this paper.

Data Availability

Data will be made available on request.

Acknowledgments

This work is supported by the National Major Science and Technology Project of China (J2019-IV-0014-0082), the National Natural Science Foundation of China (Grant Nos. 51927801, 51875574 and U2032205), 111 Project 2.0 (BP0618008), the Structural Metal Alloys Program (Grant reference No.: A18b1B0061) of the Agency for Science, Technology and Research of Singapore and the Start-up research grant (SRG/2020/000095) of SERB, DST, GoI. We appreciate the support from the International Joint Laboratory for Micro/Nano Manufacturing and Measurement Technologies and the Collaborative Innovation Center of High-End Manufacturing Equipment. W.Z. acknowledges the financial support from the program of China Scholarship Council (No. 201906280170). We also thank Dr. Yuanbin Qin for TEM characterization and Instrumental Analysis Center of Xi'an Jiaotong University for the assistance with EBSD tests.

References

Ardeljan, M., Beyerlein, I.J., Knezevic, M., 2017. Effect of dislocation density-twin interactions on twin growth in AZ31 as revealed by explicit crystal plasticity finite element modeling. Int. J. Plast. 99, 81–101.

Aubry, S., Rhee, M., Hommes, G., Bulatov, V.V., Arsenlis, A., 2016. Dislocation dynamics in hexagonal close-packed crystals. J. Mech. Phys. Solids 94, 105–126.

Bao, L., Zhang, Y., Schuman, C., Lecomte, J., Philippe, M., Zhao, X., Esling, C., 2013. Multiple twinning in pure hexagonal close-packed titanium. J. Appl. Crystallogr. 46 (5), 1397–1406.

Bisht, A., Kalsar, R., Adak, A., Dey, I., Jana, K., Lad, A., Kumar, G.R., Jagadeesh, G., Suwas, S., 2018. Observation of ex-situ microstructure relaxation of non-conventional misorientations post femtosecond laser shock exposure in cp-Ti. Acta Mater. 150, 161–172.

Chichili, D.R., Ramesh, K.T., Hemker, K.J., 1998. The high-strain-rate response of alpha-titanium: experiments, deformation mechanisms and modeling. Acta Mater. 46 (3), 1025–1043.

Choi, S., Jeong, J.S., Won, J.W., Hong, J.K., Choi, Y.S., 2021. Grade-4 commercially pure titanium with ultrahigh strength achieved by twinning-induced grain refinement through cryogenic deformation. J. Mater. Sci. Technol. 66, 193–201.

Choi, S., Won, J.W., Lee, S., Hong, J.K., Choi, Y.S., 2018. Deformation twinning activity and twin structure development of pure titanium at cryogenic temperature. Mater. Sci. Eng. A 738, 75–80.

Chun, Y.B., Yu, S.H., Semiatin, S.L., Hwang, S.K., 2005. Effect of deformation twinning on microstructure and texture evolution during cold rolling of CP-titanium. Mater. Sci. Eng. A (398), 209–219.

Clair, A., Foucault, M., Calonne, O., Lacroute, Y., Markey, L., Salazar, M., Vignal, V., Finot, E., 2011. Strain mapping near a triple junction in strained Ni-based alloy using EBSD and biaxial nanogauges. Acta Mater. 59 (8), 3116–3123.

Dai, L., Song, W., 2022. A strain rate and temperature-dependent crystal plasticity model for hexagonal close-packed (HCP) materials: Application to α-titanium. Int. J. Plast. 154, 103281.

D'Yakonov, G.S., Zherebtsov, S.V., Klimova, M.V., Salishchev, G.A., 2015. Microstructure evolution of commercial-purity titanium during cryorolling. Phys. Met. Metallogr. 2 (116), 182–188.

Fu, W., Huang, Y., Sun, J., Ngan, A.H.W., 2022. Strengthening CrFeCoNiMn0.75Cu0.25 high entropy alloy via laser shock peening. Int. J. Plast. 154, 103296.

Ghaderi, A., Barnett, M.R., 2011. Sensitivity of deformation twinning to grain size in titanium and magnesium. Acta Mater. 59 (20), 7824–7839.

Grompone Von Gioi, R., Jakubowicz, J., Morel, J., Randall, G., 2012. LSD: a line segment detector. Image Process. Line 2, 35–55.

Hamid, N., Khan, N., 2016. LSM: perceptually accurate line segment merging. J. Electron. Imaging 25 (6), 61620.

Hans, C., 1981. Effect of interstitial solutes on the strength and ductility of titanium. Prog. Mater. Sci. (26), 123–403.

Jonas, J.J., Mu, S., Al-Samman, T., Gottstein, G., Jiang, L., Martin, É., 2011. The role of strain accommodation during the variant selection of primary twins in magnesium. Acta Mater. 59 (5), 2046–2056.

Joseph, S., Lindley, T.C., Dye, D., 2018. Dislocation interactions and crack nucleation in a fatigued near-alpha titanium alloy. Int. J. Plast. 110, 38–56.

Kumar, P., Ramamurty, U., 2020. High cycle fatigue in selective laser melted Ti-6Al-4V. Acta Mater. 194, 305–320.

Lainé, S.J., Knowles, K.M., 2015. $\{11\bar{2}4\}$ deformation twinning in commercial purity titanium at room temperature. Philos. Mag. 95 (20), 2153–2166.

Lainé, S.J., Knowles, K.M., Doorbar, P.J., Cutts, R.D., Rugg, D., 2017. Microstructural characterisation of metallic shot peened and laser shock peened Ti–6Al–4V. Acta Mater. 123, 350–361.

Levinson, A., Mishra, R.K., Doherty, R.D., Kalidindi, S.R., 2013. Influence of deformation twinning on static annealing of AZ31 Mg alloy. Acta Mater. 61 (16), 5966–5978.

Li, Y., Chen, K., Dang, X., Zhang, F., Tamura, N., Ku, C., Kang, H., Wenk, H., 2020. XtalCAMP: a comprehensive program for the analysis and visualization of scanning Laue X-ray micro-/nanodiffraction data. J. Appl. Crystallogr. 53 (5), 1392–1403.

Li, Y., Wan, L., Chen, K., 2015. A look-up table based approach to characterize crystal twinning for synchrotron X-ray Laue microdiffraction scans. J. Appl. Crystallogr. 48 (3), 747–757.

Lou, S., Li, Y., Zhou, L., Nie, X., He, G., Li, Y., He, W., 2016. Surface nanocrystallization of metallic alloys with different stacking fault energy induced by laser shock processing. Mater. Des. 104, 320–326.

Lu, J.Z., Wu, L.J., Sun, G.F., Luo, K.Y., Zhang, Y.K., Cai, J., Cui, C.Y., Luo, X.M., 2017. Microstructural response and grain refinement mechanism of commercially pure titanium subjected to multiple laser shock peening impacts. Acta Mater. 127, 252–266.

Luo, S., He, W., Chen, K., Nie, X., Zhou, L., Li, Y., 2018. Regain the fatigue strength of laser additive manufactured Ti alloy via laser shock peening. J. Alloys Compd. 750, 626–635.

Lütjering, G., Williams, J.C., 2007. Titanium. Springer Science & Business Media.

Morrow, B.M., Lebensohn, R.A., Trujillo, C.P., Martinez, D.T., Addessio, F.L., Bronkhorst, C.A., Lookman, T., Cerreta, E.K., 2016. Characterization and modeling of mechanical behavior of single crystal titanium deformed by split-Hopkinson pressure bar. Int. J. Plast. 82, 225–240.

Nie, X., He, W., Zang, S., Wang, X., Zhao, J., 2014. Effect study and application to improve high cycle fatigue resistance of TC11 titanium alloy by laser shock peening with multiple impacts. Surf. Coat. Technol. 253, 68–75.

Nie, X., He, W., Zhou, L., Li, Q., Wang, X., 2014. Experiment investigation of laser shock peening on TC6 titanium alloy to improve high cycle fatigue performance. Mater. Sci. Eng. A 594, 161–167.

Norfleet, D.M., Dimiduk, D.M., Polasik, S.J., Uchic, M.D., Mills, M.J., 2008. Dislocation structures and their relationship to strength in deformed nickel microcrystals. Acta Mater. 56 (13), 2988–3001.

Pantleon, W., 2008. Resolving the geometrically necessary dislocation content by conventional electron backscattering diffraction. Scr. Mater. 58 (11), 994–997.

Qin, H., Jonas, J.J., 2014. Variant selection during secondary and tertiary twinning in pure titanium. Acta Mater. 75, 198–211.

Ren, X.D., Zhou, W.F., Liu, F.F., Ren, Y.P., Yuan, S.Q., Ren, N.F., Xu, S.D., Yang, T., 2015. Microstructure evolution and grain refinement of Ti6Al4V alloy by laser shock processing. Appl. Surf. Sci. 363, 44–49.

Rolf Adams, L.B., 1994. Seeded region growing. IEEE T. Pattern Anal. Mach. Intell. 16, 641–647.

Sahu, V.K., Yadava, M., Chakraborty, P., Gurao, N.P., 2022. Effect of notch severity and crystallographic texture on local deformation and damage in commercially pure titanium. Int. J. Plast. 155, 103318.

Singh, G., Ramamurty, U., 2020. Boron modified titanium alloys. Prog. Mater. Sci. 111, 100653.

Sinha, S., Gurao, N.P., 2017. In situ electron backscatter diffraction study of twinning in commercially pure titanium during tension-compression deformation and annealing. Mater. Des. 116, 686–693.

Spanrad, S., Tong, J., 2011. Characterisation of foreign object damage (FOD) and early fatigue crack growth in laser shock peened Ti–6Al–4V aerofoil specimens. Mater. Sci. Eng. A 528 (4-5), 2128–2136.

Sun, R., Li, L., Guo, W., Peng, P., Zhai, T., Che, Z., Li, B., Guo, C., Zhu, Y., 2018. Laser shock peening induced fatigue crack retardation in Ti-17 titanium alloy. Mater. Sci. Eng. A 737, 94–104.

Tabor, D., 1951. The Hardness of Metals. Clarendon Press, Oxford.

Tang, J., Fan, H., Wei, D., Jiang, W., Wang, Q., Tian, X., Zhang, X., 2020. Interaction between a{101ℏ2} twin boundary and grain boundaries in magnesium. Int. J. Plast. 126, 102613.

Tiamiyu, A.A., Tari, V., Szpunar, J.A., Odeshi, A.G., Khan, A.K., 2018. Effects of grain refinement on the quasi-static compressive behavior of AISI 321 austenitic stainless steel: EBSD, TEM, and XRD studies. Int. J. Plast. 107, 79–99.

Wang, F., Agnew, S.R., 2016. Dislocation transmutation by tension twinning in magnesium alloy AZ31. Int. J. Plast. 81, 63–86.

Wang, J., Beyerlein, I.J., Tomé, C.N., 2014. Reactions of lattice dislocations with grain boundaries in Mg: Implications on the micro scale from atomic-scale calculations. Int. J. Plast. 56, 156–172.

Wang, Y., He, W., Liu, N., Chapuis, A., Luan, B., Liu, Q., 2018. Effect of pre-annealing deformation on the recrystallized texture and grain boundary misorientation in commercial pure titanium. Mater. Charact. 136, 1–11.
Xiong, Y., Karamched, P., Nguyen, C., Collins, D.M., Magazzeni, C.M., Tarleton, E., Wilkinson, A.J., 2020. Cold creep of titanium: Analysis of stress relaxation using synchrotron diffraction and crystal plasticity simulations. Acta Mater. 199, 561–577.
Xu, F., Zhang, X., Ni, H., Liu, Q., 2012. Deformation twinning in pure Ti during dynamic plastic deformation. Mater. Sci. Eng. A 541, 190–195.
Xu, S., Zhou, P., Liu, G., Xiao, D., Gong, M., Wang, J., 2019. Shock-induced two types of $\{10\bar{1}2\}$ sequential twinning in Titanium. Acta Mater. 165, 547–560.
Yang, Y., Zhang, H., Qiao, H., 2017. Microstructure characteristics and formation mechanism of TC17 titanium alloy induced by laser shock processing. J. Alloys Compd. 722, 509–516.
Zhang, X., Li, C., 2017. The effect of loading rate on deformation of TA1 titanium alloy bars subjected to electromagnetic heading. Mater. Sci. Eng. A 679, 511–519.
Zhao, J., Wang, K., Huang, K., Liu, G., 2019. Recrystallization behavior during hot tensile deformation of TA15 titanium alloy sheet with substantial prior deformed substructures. Mater. Charact. 151, 429–435.
Zhao, Z., Wang, L., Lu, K., Li, Y., Chen, W., Liu, L., 2020. Effect of foreign object damage on high-cycle fatigue strength of titanium alloy for aero-engine blade. Eng. Fail. Anal. 118, 104842.
Zhou, G., Zhang, Y., Pantleon, W., Kou, J., Ramamurty, U., Tan, X., Chen, K., 2022. Quantification of room temperature strengthening of laser shock peened Ni-based superalloy using synchrotron microdiffraction. Mater. Des. 221, 110948.
Zhou, L., He, W., Luo, S., Long, C., Wang, C., Nie, X., He, G., Shen, X., Li, Y., 2016. Laser shock peening induced surface nanocrystallization and martensite transformation in austenitic stainless steel. J. Alloys Compd. 655, 66–70.
Zhou, L., Li, Y., He, W., He, G., Nie, X., Chen, D., Lai, Z., An, Z., 2013. Deforming TC6 titanium alloys at ultrahigh strain rates during multiple laser shock peening. Mater. Sci. Eng. A 578, 181–186.
Zuiderveld, K., 1994. VIII.5. - contrast limited adaptive histogram equalization. Heckbert, P.S. Graphics Gems. Academic Press, pp. 474–485.